


 Cite this: *RSC Adv.*, 2025, **15**, 47231

# Activated carbon synthesised from lignocellulosic cocoa pod husk *via* alkaline and acid treatment for methylene blue adsorption: optimisation by response surface methodology, kinetics, and isotherm modelling

Zenaida Guerra-Que, <sup>a</sup> Katia S. López-Margalli, <sup>a</sup> Juan Manuel Urrieta-Saltijeral, <sup>a</sup> Adib Abiu Silahua-Pavón, <sup>a</sup> Héctor Martínez-García, <sup>a</sup> Pedro García-Alamilla, <sup>b</sup> Gerardo E. Córdova-Pérez, <sup>c</sup> Juan Carlos Arévalo-Pérez <sup>d</sup> and José Gilberto Torres-Torres <sup>d</sup>

This study reports the green synthesis of activated carbon (ANC) from Cocoa Pod Husk (CPH), a lignocellulosic agrowaste, using sulphuric acid and sodium hydroxide treatments for Methylene Blue (MB) removal. Among the synthesised samples, ANCSH5 (NaOH, 5 M) exhibited superior performance due to extensive delignification, enhanced graphitization, and an abundance of oxygenated functionalities, as confirmed by Fourier Transform Infrared (FTIR), Scanning Electron Microscopy – Energy Dispersive X-ray (SEM-EDX), the Brunauer–Emmett–Teller Method (BET), X-ray Diffraction (XRD), Point of Zero Charge (pH<sub>PZC</sub>), and Raman analyses. ANCSH5 achieved 92% MB removal (1.16 mg g<sup>-1</sup>), surpassing CPH (24%, 0.30 mg g<sup>-1</sup>) and ANCSA10 (44%, 0.50 mg g<sup>-1</sup>). Adsorption followed pseudo-second-order kinetics, while equilibrium data fitted best to the Freundlich, Sips, Toth, and Redlich–Peterson models ( $R^2 > 0.999$ ). Process optimisation *via* a central composite design (CCD) and Response Surface Methodology (RSM) determined optimal conditions (49.6 °C, pH 6.0), achieving a 99.05% removal rate. Importantly, isotherm modelling predicted a competitive  $q_{\max}$  of 100 mg g<sup>-1</sup> for ANCSH5 under practical conditions. Unlike conventional biomass carbons, the hemicellulose-rich CPH precursor promoted extensive delignification, partially graphitised domains, and tailored surface chemistry, providing a distinctive adsorption mechanism. These features underscore CPH valorisation as a sustainable route to high-performance, low-cost adsorbents for dye remediation in cocoa-producing regions.

Received 31st July 2025  
 Accepted 13th November 2025  
 DOI: 10.1039/d5ra05557a  
[rsc.li/rsc-advances](http://rsc.li/rsc-advances)

## 1 Introduction

Access to clean and safe water has become a critical global challenge, as less than 1% of the earth's total water supply is

available as freshwater from rivers, lakes, and aquifers.<sup>1</sup> Industrial discharges, particularly from the textile, paper, and leather industries, contribute significantly to environmental degradation and pose risks to both human health and aquatic ecosystems.<sup>2–5</sup> Among the priority pollutants, synthetic dyes have been classified as persistent organic pollutants (POPs) under the Stockholm Convention, owing to their high chemical stability, toxicity, and poor biodegradability.<sup>6–8</sup>

Methylene blue (MB) is a widely used cationic dye in textile and paper processing, whose release into aquatic environments can cause carcinogenic, mutagenic, and ecotoxic effects.<sup>9–11</sup> Due to its complex aromatic structure (Fig. 1), MB is resistant to conventional treatment methods (biological or physicochemical), which are often inefficient or economically unsustainable.<sup>12,13</sup> In this context, adsorption onto Activated Carbon (AC) has emerged as a cost-effective and efficient alternative compared to other technologies such as ion exchange, membrane filtration, or photocatalysis.<sup>13–15</sup>

<sup>a</sup>Tecnológico Nacional de México-Instituto Tecnológico de Villahermosa (TECNM – I. T. Villahermosa), Laboratorio de Investigación 1 Área de Nanotecnología, Km. 3.5 Carretera Villahermosa-Frontera, Cd. Industrial, C.P. 86010 Villahermosa, Tabasco, Mexico. E-mail: zenaida.gq@villahermosa.tecnm.mx; zenaida.guerra4@gmail.com; Tel: +52 9933046111

<sup>b</sup>División Académica de Ciencias Agropecuarias (DACA), Universidad Juárez Autónoma de Tabasco (UJAT), Carret. Villahermosa-Teapa Km 25, Ra. La Huasteca, Tabasco, 86280, Mexico

<sup>c</sup>Benemérita Universidad Autónoma de Puebla, Facultad de Ciencias químicas, Centro Avanzado de Pruebas Analíticas no Destructivas, 72570 Puebla, Mexico

<sup>d</sup>Universidad Juárez Autónoma de Tabasco, Centro de Investigación de Ciencia y Tecnología Aplicada (CICTAT), DACB, Laboratorio de Nanomateriales Catalíticos Aplicados al Desarrollo de Fuentes de Energía y Remediación Ambiental, Km.1 carretera Cunduacán-Jalpa de Méndez, Cunduacán, Tabasco, C.P. 86690, Mexico



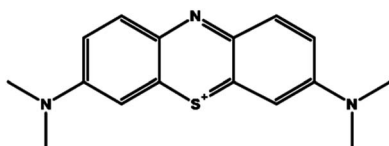


Fig. 1 Molecular structure of MB dye.

In developing countries such as Mexico, wastewater from the textile industry is often discharged directly into rivers and other natural water bodies, either untreated or insufficiently treated.<sup>16,17</sup> This practice significantly contributes to the deterioration of aquatic ecosystems and highlights the urgent need for cost-effective and sustainable wastewater treatment technologies.

Cocoa Pod Husk (CPH), an abundant agro-industrial waste in cocoa-producing regions such as Mexico, represents a largely underutilised precursor for carbon production. For every ton of dry cocoa beans, approximately 10 tons of CPH are discarded, generating a significant environmental burden.<sup>18–24</sup> According to the Mexican Agriculture Public Organization (MAPO, 2022),<sup>25</sup> about 28 000 tonnes of cocoa beans were produced in 2021, corresponding to nearly 280 000 tonnes of CPH waste. The lignocellulosic composition of CPH, rich in hemicellulose, lignin, and cellulose, makes it an attractive candidate for chemical activation and valorisation into carbon-based nanomaterials.<sup>18–21</sup> Unlike other biomass sources,<sup>26–32</sup> the high hemicellulose fraction of CPH facilitates delignification, enabling the formation of nanocarbon domains with distinct surface functionalities.

In particular, CPH has been reported as a promising feedstock in recent studies, confirming its potential for removing organic pollutants from water.<sup>21,23,33,34</sup> The development of carbon-based materials has also been highlighted in other contexts, such as polymeric composites and structural applications, demonstrating the versatility and broad applicability of carbon materials.<sup>35</sup> Nevertheless, limitations remain regarding pore efficiency under variable operating conditions. Moreover, few studies have applied robust statistical design approaches such as Response Surface Methodology (RSM) to optimise critical process parameters simultaneously.

In this work, we applied two independent chemical activation strategies, alkaline ( $\text{NaOH}$ ) and acidic ( $\text{H}_2\text{SO}_4$ ), to CPH, a non-conventional lignocellulosic precursor, to synthesise Activated Carbon (ANC). Unlike conventional biomass precursors such as rice husk or coconut shell, CPH possesses a uniquely high hemicellulose-to-lignin ratio, which enables more extensive delignification and the development of partially graphitised domains enriched with oxygen-containing functionalities.<sup>18,20,36,37</sup> These distinctive structural and chemical transformations differentiate CPH-derived ANC from previously reported biomass-based carbons, providing higher graphitization and enhanced adsorption performance.<sup>38–41</sup> The resulting materials were comprehensively characterised to elucidate surface chemistry and textural evolution, while adsorption toward MB was evaluated through kinetic and equilibrium modelling. Furthermore, process optimisation was performed

using central composite design (CCD) and RSM, a method that has not been systematically applied to CPH-derived carbons. Beyond performance, this study highlights the green valorisation of an abundant agro-waste into chemically activated adsorbents, aligning with circular economy principles. By coupling enhanced graphitisation with optimised adsorption efficiency, the proposed approach highlights the green valorisation of an abundant agro-waste into chemically activated adsorbents, aligning a sustainable and cost-effective solution for wastewater remediation in cocoa-producing regions.

## 2 Methods

### 2.1 Precursor material

The CPH utilized in this study were collected from the farm of Mr Efrén Hernández Maldonado, located in Ra. Mihuatlán, Cunduacán, Tabasco, México. The farm supplies raw materials to Chocolatería Artesanal Citlalli, owned by Mr Cutberto Lázaro Cepeda.

The raw material, referred to as CPH, comprised 4 kg of agricultural waste. The husks were thoroughly washed multiple times with deionized water to remove dust and surface impurities. Subsequently, the material was air-dried under sunlight for three days on a flat, open surface, followed by oven drying at 100 °C for 48 hours using a Riessa oven (Riessa, Mexico). After drying, the material was ground and sieved to obtain particles smaller than 0.25 mm (mesh size 60–80), using a conventional mechanical sieve shaker. Similar pre-treatment steps have been widely reported for lignocellulosic precursors to ensure homogeneity and surface cleanliness prior to activation.<sup>15,23,24</sup> The resulting CPH powder was subjected to the determination of extractives, cellulose, hemicellulose, and lignin contents following the standard analytical protocols reported in the Official Methods of Analysis of AOAC International (18th ed.),<sup>42</sup> in accordance with the acid-alkali digestion and solvent extraction procedures commonly employed for lignocellulosic residues [Sluiter *et al.*, NREL/TP-510-42618, 2012].<sup>43</sup> Comparable pre-treatment and characterisation methodologies for lignocellulosic precursors have also been reported by Selvaraju and Bakar (2017)<sup>44</sup> and Li *et al.* (2014),<sup>45</sup> whose studies are widely cited and validate the reliability of these analytical techniques.

### 2.2 Lignocellulosic characterisation of cocoa pod husk (CPH) before treatment

The structural composition of lignocellulosic biomass, particularly the arrangement of cellulose, hemicellulose, and lignin, plays a crucial role in determining the reactivity of the precursor and its subsequent activation performance. For clarity, the molecular structure of cellulose is shown in Fig. 2 as a representative component of the lignocellulosic framework in CPH.

**2.2.1 Determination of extractives content.** The Cocoa Pod Husk Powder (CPHP,  $W_0$ ) was mixed with a benzene/ethanol solution (2 : 1 v/v) and maintained at a constant temperature for 3 hours to extract soluble components. The mixture was then filtered, and the solid residue was dried in an oven at 105 °



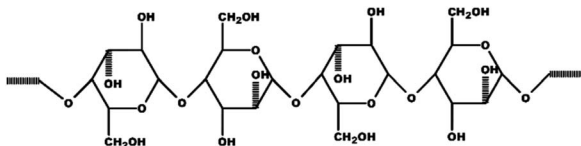


Fig. 2 Molecular structure of cellulose, representative of lignocellulosic components in CPH.

C for 24 hours until a constant weight was achieved. After cooling to room temperature in a desiccator, the sample was weighed ( $W_1$ ). The extractable content (% Ext) was calculated using eqn (1):

$$\% \text{ Ext} = \frac{W_0 - W_1}{W_0} \times 100 \quad (1)$$

The remaining residue was subsequently used for quantifying the hemicellulose and lignin contents.<sup>42-45</sup>

**2.2.2 Determination of hemicellulose content.** A volume of 150 mL of sodium hydroxide solution (20 g L<sup>-1</sup>) was added to the extractive-free residue ( $W_2$ ). The mixture was placed in a covered beaker and heated at a constant temperature for 3.5 hours. The resulting solid was separated by Büchner filtration and washed four times with 150 mL of distilled water to remove residual sodium ions. The solid was then dried in an oven at 105 °C for 24 hours and weighed ( $W_3$ ).<sup>42-45</sup> The hemicellulose content (% Hemi) was determined using eqn (2):

$$\% \text{ Hemi} = \frac{W_2 - W_3}{W_2} \times 100 \quad (2)$$

**2.2.3 Determination of lignin content.** A 1 g portion of the residue obtained from the extractive analysis was dried in an oven at 105 °C until constant weight and then cooled in a desiccator before being weighed ( $W_4$ ). Subsequently, 30 mL of concentrated sulphuric acid (72% H<sub>2</sub>SO<sub>4</sub>) was slowly added to the sample. The mixture was maintained at a temperature between 8 and 15 °C for 24 hours. After this period, the sample was transferred to a flask, diluted with 300 mL of distilled water, and heated to a boil for 1 hour. The resulting residue was filtered, thoroughly washed to remove residual sulfate ions, dried at 50 °C to constant weight, cooled in a desiccator, and finally weighed ( $W_5$ ).<sup>42-45</sup> The lignin content (% Lignin) was calculated using eqn (3):

$$\% \text{ Lignin} = \frac{W_5}{W_4} \times (100 - \% \text{ Ext}) \quad (3)$$

**2.2.4 Determination of cellulose content (by difference).** The cellulose content (% Cellulose) was determined by difference, using eqn (4):

$$\% \text{ Cellulose} = 100 - \% \text{ Ext} - \% \text{ Hemi} - \% \text{ Lignin} \quad (4)$$

**2.2.5 Proximate analysis of CPHP.** Proximate analysis was carried out by the official methods of the Association of Official

Analytical Chemists (AOAC, 2005),<sup>42</sup> including moisture content (Method 925.09), crude fat (920.30), crude protein (979.09), ash (923.03), and crude fiber (962.09). Carbohydrate content was calculated by difference.

### 2.3 Green synthesis of ANC from CPH powder

The delignification process for material synthesis was conducted *via* immersion in alkaline and acidic solutions. Treatments were carried out using a 1:10 (w/v) ratio of lignocellulosic residue to chemical solution at room temperature for 12 hours, with two concentration levels applied for each condition. For alkaline activation, CPHP, previously oven-dried, was immersed in sodium hydroxide solutions at concentrations of 0.1 M and 5 M (solid-to-liquid ratio of 100 g L<sup>-1</sup>). The resulting samples were designated as ANCSH0.1 and ANCSH5, respectively. Similarly, acidic treatment was performed by immersing CPHP in sulphuric acid solutions at 0.5 M and 10 M concentrations, yielding samples labelled ANCSA0.5 and ANCSA10. After treatment, all suspensions were vacuum-filtered and thoroughly washed with deionised water until the filtrate reached a neutral pH, followed by rinsing with acetone. The treated solids were then oven-dried at 80 °C until constant weight was achieved, typically within 24 hours. Previous studies have demonstrated the effectiveness of alkali and acid pretreatments in modifying CPH for enhanced dye adsorption, particularly sodium hydroxide delignification to improve surface reactivity and porosity.<sup>20,23,24,33,34,36</sup>

#### 2.3.1 Characterisation of ANC synthesised from CPH

**2.3.1.1 N<sub>2</sub> adsorption-desorption isotherm.** The specific surface area, pore diameter, and pore volume of the CPH and ANC samples were determined *via* N<sub>2</sub> physisorption using a Micromeritics TriStar II 3020 surface area analyzer at 77 K (-196 °C). Before analysis, approximately 0.1 g of each sample was degassed at 300 °C for 3 hours to remove adsorbed impurities and moisture. The obtained adsorption-desorption isotherms were analyzed using the Brunauer-Emmett-Teller (BET) method to calculate the specific surface area ( $S_{\text{BET}}$ ), while pore volume ( $P_v$ ) and average pore diameter ( $P_s$ ) were determined using the Barrett-Joyner-Halenda (BJH) model as implemented in the ASAP 2020 software package.<sup>32,36,41</sup>

**2.3.1.2 Scanning electron microscopy (SEM) and energy-dispersive X-ray spectroscopy (EDX).** SEM was conducted using a JEOL/EO JSM-6610 microscope operated at 5–20 kV and equipped with EDX. Before imaging, samples were sputter-coated with a thin layer of gold to enhance surface conductivity. A small amount of powdered sample was mounted on carbon adhesive tape fixed to aluminum stubs, followed by gold coating. Micrographs were acquired at magnifications ranging from 100 $\times$  to 100 00 $\times$  to examine surface morphology and elemental distribution, which are critical parameters in evaluating biomass-derived carbons.<sup>46</sup> The characterisation was conducted at the Center for Research in Science and Applied Technology of Tabasco (CICAT), Academic Division of Basic Sciences, Universidad Juárez Autónoma de Tabasco (UJAT), in collaboration with the Faculty of Chemical Sciences



at Benemérita Universidad Autónoma de Puebla (BUAP), with technical support from Dr Gerardo Enrique Córdova Pérez.

**2.3.1.3 X-Ray diffraction (XRD).** XRD analysis was performed to identify the crystalline phases and estimate the crystallite sizes of the CPH and ANC samples. Measurements were conducted using a Bruker D2 PHASER diffractometer equipped with a Co K $\alpha$  radiation source ( $\lambda = 0.179$  nm). Diffraction patterns were collected over a  $2\theta$  range of  $20^\circ$  to  $80^\circ$  with a total scan time of 660 seconds. Phase identification was performed using the JADE 6 software and the corresponding database. The interpretation of structural ordering in carbonaceous materials through XRD is consistent with previously reported studies on lignocellulosic biomass-derived carbons.<sup>47,48</sup>

The average crystallite size was estimated using the Scherrer eqn (5).

$$D = \frac{0.90\lambda}{\beta \cos \theta} \quad (5)$$

where  $\lambda$  represents the X-ray wavelength,  $\beta$  the full width at half maximum (FWHM), and  $\theta$  the Bragg angle. This approach has been widely applied for the estimation of crystalline domain sizes in biomass-derived carbons and related disordered carbon materials.<sup>47,49</sup>

**2.3.1.4 Raman spectroscopy.** Raman spectroscopy was employed to identify vibrational modes in CPH and ANC samples. The measurements were conducted using a HORIBA Xplora Plus Raman microscope equipped with a He-Ne laser ( $\lambda = 632.8$  nm, 16 mW). The system featured spatial resolutions of 20, 5, and 2  $\mu\text{m}$ , and a spectral resolution ranging from  $\pm 0.2$  to  $\pm 0.5 \text{ cm}^{-1}$ . The instrument was equipped with a thermoelectrically cooled CCD detector, an optical microscope with objectives of  $10\times$ ,  $50\times$ , and  $100\times$ , and an integrated video camera for sample focusing. A motorised sample stage enabled mapping over a maximum area of  $5 \text{ mm}^2$ . Raman spectroscopy is widely recognised as a powerful tool for probing structural order, bonding, and defect density in carbon-based materials, as extensively discussed in both classical and recent studies.<sup>48,50</sup>

**2.3.1.5 Fourier Transform Infrared Spectroscopy (FTIR).** FTIR spectroscopy was performed using a PerkinElmer Frontier spectrophotometer (USA) equipped with a Diamond Attenuated Total Reflection (ATR) accessory and operated *via* Windows®-based software. Spectra were recorded in the wavenumber range of  $400\text{--}4000 \text{ cm}^{-1}$  with a resolution of  $4 \text{ cm}^{-1}$ , averaging 32 scans per spectrum. Samples analysed included untreated CPH, CPH after acid and alkaline treatments, and the corresponding ANC materials. Each spectrum was subjected to baseline correction, smoothing, and normalization using PerkinElmer Spectrum software. All measurements were performed in triplicate, and the resulting spectral data were processed and visualised using OriginPro 8.5.1. FTIR spectroscopy has been widely employed for identifying functional groups and monitoring surface modifications in biomass-derived carbons, providing key insights into chemical transformations during acid and alkaline pretreatments.<sup>28,46</sup>

**2.3.1.6 Point of zero charge ( $\text{pH}_{\text{PZC}}$ ) determination.** The  $\text{pH}_{\text{PZC}}$  of the adsorbents was determined using the pH-drift method. In brief, 50 mL of 0.01 M NaCl solution was placed in a series of

closed Erlenmeyer flasks, and the initial pH ( $\text{pH}_i$ ) of each solution was adjusted to values between 2.0 and 12.0 using 0.1 M HCl or 0.1 M NaOH. A fixed mass of adsorbent (0.05 g) was then added, and the suspensions were shaken at room temperature for 24 hours to reach equilibrium. The final pH ( $\text{pH}_f$ ) of each solution was recorded, and the difference ( $\Delta\text{pH} = \text{pH}_f - \text{pH}_i$ ) was plotted as a function of  $\text{pH}_i$ . The pH at which  $\Delta\text{pH} = 0$  was taken as the  $\text{pH}_{\text{PZC}}$ , representing the condition at which the adsorbent surface exhibits no net charge. This procedure has been extensively used for biomass-derived carbons to elucidate surface charge properties and their role in dye adsorption.<sup>38,51-53</sup>

## 2.4 Adsorption experiments

The adsorption performance of the five adsorbent samples, CPH, ANCSH0.1, ANCSH5, ANCSA0.5, and ANCSA10, was evaluated through batch adsorption studies using MB as a model pollutant. Experimental conditions (solid–liquid ratio, initial concentration range, pH window, contact time, and temperature) followed widely adopted protocols for MB adsorption on biomass-derived activated carbons,<sup>14,40</sup> including CPH-based systems.<sup>24</sup> For isotherm studies, 400 mg of each adsorbent was added to 100 mL of MB solution at an initial concentration of 5 to 30 mg L<sup>-1</sup> and pH 6. The effects of contact time (30–180 min), temperature (35–65 °C), and pH (2–6) on MB removal were systematically assessed in line with prior reports on MB adsorption using plant-waste-derived carbons.<sup>51,54-56</sup> After each adsorption run, samples were vacuum-filtered using 1.2  $\mu\text{m}$  glass microfiber filters. In kinetic experiments, MB concentration was monitored at defined time intervals to resolve uptake profiles, enabling pseudo-order rate modelling and subsequent parameter estimation as commonly applied for MB on hydrochars and agrowaste carbons.<sup>5,57</sup> MB concentrations before and after adsorption were quantified by UV-Vis spectroscopy (Agilent Technologies, Varian Cary 3000, USA) with  $\lambda_{\text{max}}$  at 663 nm, consistent with standard MB quantification protocols for lignocellulosic carbons.<sup>51,54-56</sup> Thermodynamic parameters ( $\Delta G^\circ$ ,  $\Delta H^\circ$ ,  $\Delta S^\circ$ ) were calculated from equilibrium constants ( $K_c = q_e/C_e$ ) using the van't Hoff and Gibbs equations, as described in Section 3.3.3. All experiments were performed in duplicate, and each measurement was performed in triplicate to ensure reproducibility.

The adsorption capacity at equilibrium,  $q_e$  (mg g<sup>-1</sup>), was calculated using eqn (6):

$$q_e = \frac{(C_0 - C_e)V}{W} \quad (6)$$

where  $C_0$  is the initial concentration of MB (mg L<sup>-1</sup>);  $C_e$  is the concentration of MB at equilibrium (mg L<sup>-1</sup>),  $V$ , the volume of the solution (L), and  $W$ , the mass of the adsorbent used (g).<sup>14,51</sup>

The following expression was used to calculate the dye removal percentage.

$$R \% = \frac{(C_0 - C_e)}{C_0} \times 100 \quad (7)$$



**2.4.1 Adsorption kinetics.** Exploring adsorption kinetics models provides critical insights into the mechanisms that govern MB uptake onto CPH, ANCSH0.1, ANCSH5, ANCSA0.5, and ANCSA10. Investigating the adsorption rate and the time required to attain equilibrium is essential for evaluating and characterizing the adsorption performance of these materials.<sup>58,59</sup> In this study, the experimental kinetic data were fitted to two widely used models: the pseudo-first-order and pseudo-second-order kinetic models, to identify the potential rate-limiting steps and gain a better understanding of the adsorption dynamics.

The pseudo-first-order kinetic model<sup>15</sup> is expressed in linear form in eqn (8).

$$\ln(q_e - q_t) = \ln q_e - k_1 t \quad (8)$$

And the nonlinear form is given by ref. 54:

$$q_t = q_e(1 - e^{-k_1 t}) \quad (9)$$

where  $q_e$  (mg g<sup>-1</sup>) is the amount of adsorbate at equilibrium,  $q_t$  (mg g<sup>-1</sup>) is the amount of adsorbate adsorbed at time  $t$  (min), and  $k_1$  (min<sup>-1</sup>) is the pseudo-first-order rate constant.

The pseudo-second-order kinetic model<sup>60</sup> in linear form is given by:

$$\frac{t}{q_t} = \frac{1}{k_2 q_e^2} + \frac{t}{q_e} \quad (10)$$

where  $k_2$  (g mg<sup>-1</sup> min<sup>-1</sup>) is the pseudo-second-order rate constant.

The nonlinear form of the pseudo-second-order kinetic model<sup>61</sup> is exposed in the following eqn (11).

$$q_t = \frac{q_e^2 k_2 t}{1 + q_e k_2 t} \quad (11)$$

where the variables are the same as in the linear form.

These models assume different adsorption mechanisms: the pseudo-first-order model is typically associated with physisorption. In contrast, the pseudo-second-order model suggests chemisorption involving valence forces through sharing or exchange of electrons between the adsorbent and adsorbate.<sup>41,62</sup> The data were processed using Origin 8.5 software. By analysing the kinetic parameters and coefficient of determination ( $R^2$ ), the best-fitting model can be determined, offering valuable insights into the controlling mechanism of the adsorption process.

**2.4.2 Isotherm experiments.** The adsorption isotherm describes the equilibrium relationship between the amount of adsorbate retained on the adsorbent surface and its concentration remaining in the solution at a constant temperature.<sup>63</sup> Several adsorption isotherm models are available to analyse experimental data and describe equilibrium adsorption behavior.<sup>64</sup> In this study, the Langmuir and the Freundlich models were applied to evaluate the adsorption characteristics. In addition to these classical isotherms, the Temkin, Redlich-Peterson, Sips, and Toth models were employed, as they account for surface heterogeneity, energetic variability, and

cooperative adsorption effects, particularly relevant when working with bio-based or chemically modified adsorbents.

The Langmuir isotherm<sup>64</sup> assumes monolayer adsorption onto a surface with a finite number of identical sites and no interaction between adsorbed molecules. It is expressed as:

$$q_e = \frac{q_{\max} K_L C_e}{1 + K_L C_e} \quad (12)$$

where  $q_e$  is the amount of adsorbate adsorbed at equilibrium (mg g<sup>-1</sup>),  $q_{\max}$  is the maximum adsorption capacity corresponding to complete monolayer coverage (mg g<sup>-1</sup>),  $C_e$  is the equilibrium concentration of the adsorbate in solution (mg L<sup>-1</sup>),  $K_L$  is the Langmuir equilibrium constant related to the affinity of binding sites (L mg<sup>-1</sup>).

The Freundlich isotherm<sup>54</sup> is an empirical model that describes adsorption onto heterogeneous surfaces with a non-uniform distribution of heat of adsorption. Its eqn (13) is given by:

$$q_e = K_F C_e^{1/n} \quad (13)$$

where  $q_e$  is the amount of adsorbate adsorbed at equilibrium (mg g<sup>-1</sup>),  $K_F$  is the Freundlich constant indicative of the adsorption capacity (mg<sup>1-1/n</sup> g<sup>-1</sup> L<sup>1/n</sup>),  $C_e$  is the equilibrium concentration of the adsorbate in solution (mg L<sup>-1</sup>),  $n$  is the heterogeneity factor (dimensionless), where values of  $1 < n < 10$  indicate favorable adsorption.

The Redlich-Peterson model<sup>65</sup> combines the features of both Langmuir and the Freundlich isotherms, offering flexibility for heterogeneous or hybrid adsorption systems. Its general form is:

$$q_e = \frac{K_R C_e}{1 + a_R C_e^g} \quad (14)$$

where  $q_e$  is the amount of adsorbate adsorbed at equilibrium (mg g<sup>-1</sup>),  $K_R$  (L g<sup>-1</sup>) and  $a_R$  are Redlich-Peterson constants,  $C_e$  is the equilibrium concentration of the adsorbate in solution (mg L<sup>-1</sup>),  $g$  is the heterogeneity factor (dimensionless), with  $0 < g \leq 1$ .

The Sips isotherm<sup>24</sup> describes adsorption on heterogeneous surfaces and reduces to the Langmuir equation at low concentrations. Its eqn (15) is:

$$q_e = \frac{q_{\max} (K_s C_e)^n}{1 + K_s C_e^n} \quad (15)$$

where  $q_{\max}$  is the maximum adsorption capacity (mg g<sup>-1</sup>),  $K_s$  is the Sips isotherm constant related to adsorption intensity (L mg<sup>-1</sup>).  $n$  is the heterogeneity factor (dimensionless), with  $n = 1$  reducing the equation to Langmuir.

The Temkin model<sup>63</sup> accounts for adsorbate-adsorbent interactions and assumes the heat of adsorption decreases linearly with surface coverage. The eqn (16) is:

$$q_e = B \ln(AC_e) \quad (16)$$

$A$  is the Temkin isotherm equilibrium binding constant (L g<sup>-1</sup>),  $B = \frac{RT}{b_T}$ , where  $b_T$  is a constant related to the heat of adsorption (J mol<sup>-1</sup>),  $R$  is the universal gas constant (8.314 J mol<sup>-1</sup> K<sup>-1</sup>),  $T$  is the absolute temperature (K).

The Toth isotherm<sup>66</sup> is an empirical model used to describe adsorption on heterogeneous surfaces. It reduces to Langmuir when the heterogeneity parameter  $t = 1$ . The eqn (17) is:

$$q_e = \frac{q_{\max} K_T C_e}{(1 + (K_T C_e)^t)^{1/t}} \quad (17)$$

$q_{\max}$  is the maximum adsorption capacity ( $\text{mg g}^{-1}$ ),  $K_T$  is the Toth equilibrium constant ( $\text{L mg}^{-1}$ ),  $t$  is the Toth heterogeneity parameter (dimensionless).

## 2.5 Experimental design and optimisation studies

In this study, a CCD was employed to evaluate the main effects of two experimental variables pH (2–7) and temperature (29–71 °C), as well as their interaction effects on MB adsorption using ANCSH5 as the adsorbent. The Design Expert® software was used to perform the experimental design and RSM analysis. RSM has been widely applied to optimise adsorption processes and evaluate the combined influence of multiple operating variables on dye removal efficiency and adsorption capacity.<sup>67–72</sup> In particular, RSM and CCD approaches have proven effective in identifying optimal conditions and reducing experimental runs while maintaining statistical robustness, which justifies their application in the present work.<sup>31,67–69</sup> A CCD comprises factorial points, axial (star) points positioned at a distance  $\alpha$  from the center, and replicated center points to provide an unbiased estimate of pure error and to test for curvature.<sup>67–69,71,72</sup> Each factor is evaluated at five coded levels ( $-\alpha$ ,  $-1$ ,  $0$ ,  $+1$ , and  $+\alpha$ ), where  $\alpha$  and the number of experiments ( $N$ ) are calculated using the following equations.

$$\alpha = 2^{k/4} \quad (18)$$

$$N = 2^k + 2k + C_p \quad (19)$$

where  $k$  is the number of variables, and  $C_p$  is the number of center point replicates.<sup>67–69</sup> In many adsorption and related process-optimization studies, the response surface exhibits sufficient curvature that a first-order (linear) model is inadequate; therefore, a second-order polynomial with interaction and quadratic terms is fitted and assessed *via* ANOVA, lack-of-fit, and model adequacy diagnostics.<sup>31,68,69,71,72</sup> Therefore, to accurately identify critical points (*i.e.*, maxima or minima), a second-order polynomial model is employed, as represented in eqn (20). Quadratic models are widely recognised as essential in RSM studies because they capture surface curvature and enable the prediction of optimal conditions with high reliability.<sup>67–69,71,72</sup>

$$Y = \beta_0 + \sum_{i=1}^k \beta_i X_i + \sum_{i=1}^k \beta_{ii} X_i^2 + \sum_{i < j} \sum_j \beta_{ij} X_i X_j + \varepsilon \quad (20)$$

where  $Y$  is the predicted response;  $X_i$  and  $X_j$  are the independent variables;  $\beta_0$  is the intercept;  $\beta_i$  is the linear coefficient;  $\beta_{ii}$  is the quadratic coefficient;  $\beta_{ij}$  is the interaction coefficient between variables  $X_i$  and  $X_j$ ; and  $\varepsilon$  is the random error term.

The CCD matrix for this study consisted of 12 experimental runs, including four center points to assess reproducibility and

Table 1 CCD matrix used in the present study

Runs order	Temperature (°C)	pH
1	35	2
2	35	6
3	65	2
4	65	6
5	29	4
6	71	4
7	50	1
8	50	7
9	50	4
10	50	4
11	50	4
12	50	4

four axial points to ensure rotatability of the design (Table 1). The experimental runs were done at random to minimise systematic error. Analysis of variance (ANOVA) was used to evaluate the significance of individual and interaction effects, with main effects considered statistically significant at  $p < 0.05$  (95% confidence level). All experiments were performed in duplicate, with each measurement conducted in triplicate to ensure accuracy and statistical reliability.

Optimisation was carried out using the desirability function to identify the best pH and temperature conditions for maximum MB removal and adsorption capacity.

## 3 Results and discussion

### 3.1 Lignocellulosic characterisation of CPH before treatment

**3.1.1 Proximate and lignocellulosic composition analysis of CPH.** Table 2 summarises the lignocellulosic fractions, extractables, hemicellulose, lignin, and cellulose, as well as the proximate components, including moisture, protein, fat, ash, fiber, and carbohydrates, in CPHP, expressed as a weight percentage (wt%). Values are reported as mean  $\pm$  standard deviation.

The chemical composition of lignocellulosic bioadsorbents significantly influences their adsorption performance, as it determines the availability of functional groups and surface chemistry. CPHP is primarily composed of natural fiber polymers, with hemicellulose being the most abundant carbohydrate fraction, followed by cellulose and lignin. The cellulose content measured (19.92 wt%) is lower than values reported in other studies,<sup>39,73</sup> which may be attributed to differences in cocoa variety, cultivation practices, soil characteristics, and regional climatic conditions. In contrast, the hemicellulose content in this study was higher than that reported elsewhere, reinforcing the influence of agricultural and genetic factors on biomass composition.<sup>38,39</sup>

Additional components present in smaller quantities, such as proteins, ashes, and extractables, are grouped under “others” due to their secondary relevance in the structural composition of the biomass. Nevertheless, these constituents may still



Table 2 Physicochemical and lignocellulosic composition of CPH

Lignocellulosic composition	Content (wt%)	Proximate analysis	Content (wt%)
Extractable	13.4 ± 0.47	Humidity	9.26 ± 0.02
Hemicellulose	47.73 ± 7.84	Protein	5.29 ± 0.17
Lignin	18.95 ± 9.61	Fat	7.31 ± 0.07
Cellulose	19.92 ± 1.39	Ash (%)	8.03 ± 0.10
		Fiber	23.20 ± 1.36
		Carbohydrate	46.9 ± 0.00

contribute to the surface reactivity of the material, particularly in chemical activation and adsorption processes.<sup>38</sup>

### 3.2 Characterisation of ANC synthesised from CPH

Table 3 presents the textural parameters of the five adsorbents, determined from the  $N_2$  adsorption isotherm using the BET method. The specific surface area ( $S_{BET}$ ) increases with higher concentrations of chemical treatment, showing a significant rise with sulphuric acid. All five adsorbents are mesoporous in terms of pore size ( $P_s$ ), with ANCSH0.1 exhibiting the smallest  $P_s$ . The chemical treatment removes moisture and volatile matter from the biomass, which typically enhances its reactivity as an adsorbent.<sup>40,74</sup>

**3.2.1 Scanning electron microscopy (SEM) with energy dispersive X-ray (EDX).** Fig. 3 shows SEM images of CPH, ANCSH0.1, ANCSH5, and ANCSA10 captured at magnifications of 100 $\times$  and 1000 $\times$ . The surface morphology of CPH undergoes significant changes following chemical activation. As seen in low-magnification images, CPH initially exhibits a dense, rigid, and compact structure with a smooth surface and no visible cavities. However, after treatment with acid and alkaline agents, the morphology changes dramatically, particularly in samples ANCSH5 and ANCSA10. These chemically activated variants display rougher surfaces and a more porous structure, characterised by the development of additional pores and cracks. This transformation increases the overall surface area of the material, enhancing its potential for applications such as adsorption. The clear contrast between the untreated CPH and the acid/alkaline-treated forms underscores the effectiveness of chemical activation in modifying surface characteristics and improving functional performance.<sup>12,23,24</sup>

The predominantly quasi-spherical and rod morphology of ANCSH5 and ANCSA10 particles is evident, with most seen particles exhibiting this shape. This morphological

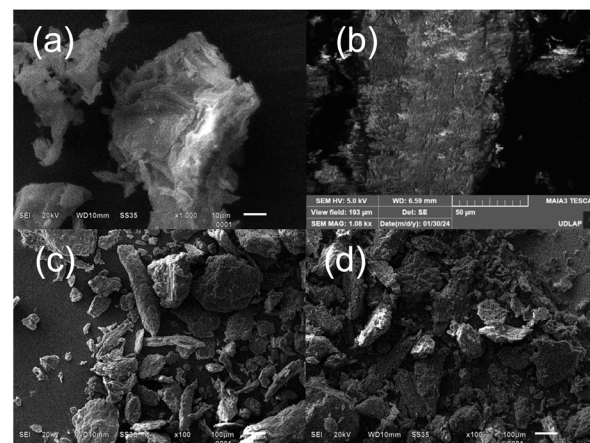


Fig. 3 SEM micrographs of (a) CPH, (b) ANCSH0.1, (c) ANCSH5, and (d) ANCSA10. Experimental conditions: accelerating voltage 5–20 kV, magnifications 100 $\times$ –1000 $\times$ .

transformation is primarily attributed to the elimination of hydrophobic waxes, pectin, hemicellulose, lignin, and other impurities from the CPH matrix during sequential acid and alkaline treatments. The defibrillation of cellulose into individual fibrils is linked to the removal of its amorphous regions, predominantly influenced by the presence of hemicellulose and lignin.<sup>18,21,27</sup> The total weight loss of the CPH, 18% after the NaOH treatment and 40% after the  $H_2SO_4$  treatment, further confirms this.

Fig. 4 shows the EDX Spectra of CPH, ANCSH5, and ANCSA10. Elemental analysis of CPH reveals the presence of carbon (47.40%), oxygen (38.32%), nitrogen (13.93%), potassium (0.15%), phosphorus (0.04%), and calcium (0.16%). However, elemental analysis of ANCSH5 and ANCSA10 reveals the presence of all elements detected in CPH, except for phosphorus, potassium, and calcium. The increased carbon peaks (Fig. 4b and c) and higher estimated mass percentages (Table 4) seen in the EDX analysis of ANCSA10 and ANCSH5, relative to CPH, indicate that the chemical treatment effectively promoted the carbonization process.

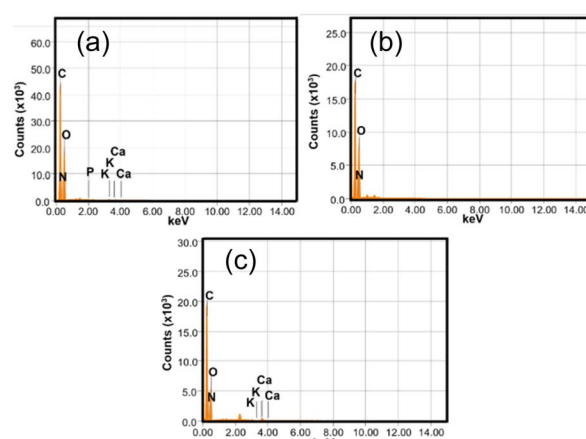


Fig. 4 EDX spectra of (a) CPH, (b) ANCSH5, and (c) ANCSA10.

Table 3 Specific surface area ( $S_{BET}$ ), pore volume ( $P_V$ ), and pore size ( $P_s$ ) of the adsorbents. N.D. not detected

Adsorbent	$S_{BET}$ ( $m^2 g^{-1}$ )	$P_V$ ( $cm^3 g^{-1}$ )	$P_s$ (nm)
CPH	0.0169	0.000778	7
ANCSA0.5	0.129	0.000366	10
ANCSA10	1.966	0.004617	14
ANCSH0.1	0.5115	0.000039	3.5
ANCSH5	0.2218	0.000511	N.D.



**Table 4** EDX semiquantitative analysis of samples: CPH, ANCSA10, and ANCSH5. N.D. not detected

Chemical element (ms%)	CPH	ANCSA10	ANCSH5
C	47.40	49.19	48.91
N	13.93	21.70	20.36
O	38.32	28.8	30.73
K	0.15	0.01	N.D.
P	0.04	N.D.	N.D.
Ca	0.16	0.30	N.D.
Total	100	100	100

Similar outcomes were obtained by Mousavi-Qeydary *et al.*<sup>75</sup> in their study of activated carbon made from human hair waste, and Putra Negara *et al.*<sup>76</sup> who synthesised activated carbons derived tabah bamboo.

**3.2.2 X-Ray Diffraction (XRD).** The XRD pattern of raw lignocellulosic CPH (Fig. 5) exhibited broad, low-intensity peaks at  $2\theta \approx 21.7^\circ$ ,  $34.4^\circ$ , and  $43.5^\circ$ , corresponding to amorphous cellulose, disordered lignin domains, and the incipient (100) graphitic plane, respectively. These features confirm the highly amorphous nature of the pristine biomass, dominated by poorly ordered carbonaceous structures.<sup>47,49,77</sup>

Significant structural transformations were seen following chemical activation. The ANCSH5 sample (treated with 5 M NaOH) displayed sharper and more intense reflections at the same positions, indicating enhanced crystallinity and a higher degree of graphitization. Notably, the increased intensity of the (100) peak at  $43.5^\circ$  suggests the formation of graphene-like  $sp^2$  carbon domains, likely due to the effective delignification and removal of hemicellulose under strong alkaline hydrolysis.<sup>48</sup>

In contrast, the ANCSA10 sample (treated with 10 M  $H_2SO_4$ ) showed additional peaks at  $29.4^\circ$  and  $31.7^\circ$ , alongside those at  $21.7^\circ$ ,  $34.4^\circ$ , and  $43.5^\circ$ . These are attributed to the formation of organosulfate or sulfonated crystalline phases, reflecting more

complex structural rearrangements. However, the broader peaks indicate that strong acid activation induced partial structural collapse, limiting long-range order.<sup>47,52</sup>

Samples treated with lower concentrations of acid (ANCSA0.5) and base (ANCSH0.1) exhibited only weak reflections at  $34.4^\circ$  and  $43.5^\circ$ , indicating limited carbon ordering and incomplete removal of amorphous constituents.

The prominent reflection at  $43.5^\circ$ , corresponding to the (100) plane of hexagonal graphite, serves as a key indicator of aromatic ring condensation and planar  $sp^2$  carbon alignment.<sup>48,78</sup> Its pronounced intensity in ANCSH5 confirms the highest degree of graphitisation among all tested materials, consistent with its enhanced physicochemical properties for adsorption applications.

**3.2.3 Raman spectroscopy.** Fig. 6 presents the Raman spectra of CPH, ANCSH0.1, ANCSH5, ANCSA0.5, and ANCSA10. The CPH sample exhibited D and G bands at  $1389\text{ cm}^{-1}$  and  $1602\text{ cm}^{-1}$ , respectively. For ANCSH0.1, the D and G bands appeared at  $1389\text{ cm}^{-1}$  and  $1611\text{ cm}^{-1}$ , while for ANCSH5, they were seen at  $1395\text{ cm}^{-1}$  and  $1608\text{ cm}^{-1}$ . In the case of ANCSA0.5, the D and G bands were located at  $1389\text{ cm}^{-1}$  and  $1605\text{ cm}^{-1}$ , respectively. ANCSA10 showed D and G bands at  $1395\text{ cm}^{-1}$  and  $1608\text{ cm}^{-1}$ .

The presence of both D and G bands in all samples confirms the carbonaceous nature of the materials, with varying degrees of structural order. The D and G bands were seen in the ranges of  $1300\text{--}1410\text{ cm}^{-1}$  and  $1550\text{--}1610\text{ cm}^{-1}$ , respectively, consistent with reported values in the literature for disordered carbon matrices.<sup>50,79,80</sup> The D band, indicative of structural disorder, exhibited the highest intensity in the raw CPH sample, reflecting a highly disordered carbon framework. In contrast, this behaviour differed in the chemically treated samples, suggesting modifications in the carbon framework due to the treatments.<sup>81-83</sup> The D band is associated with disordered carbon regions, and the G band corresponds to ordered graphitic structures. The D band arises from the breathing modes of  $sp^2$ -hybridised carbon atoms in aromatic rings and is activated by structural defects or disorder, often associated with

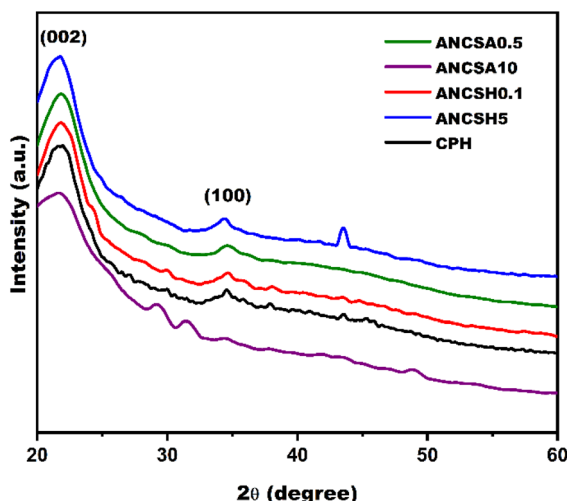


**Fig. 5** XRD patterns of raw CPH and chemically ANCs: ANCSH0.1, ANCSH5, ANCSA0.5, and ANCSA10.

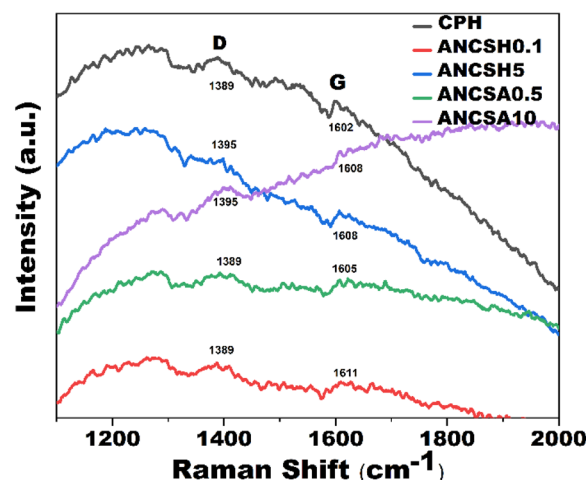


**Fig. 6** Raman spectra of CPH, ANCSH0.1, ANCSH5, ANCSA0.5, and ANCSA10. Excitation wavelength: 632.8 nm.



$sp^3$  hybridisation. In contrast, the G band results from the in-plane stretching of  $sp^2$ -hybridised carbon atoms, characteristic of ordered graphitic domains. These well-defined features in the Raman spectra offer valuable insight into the heterogeneous microstructure of the carbon materials.<sup>79,83,84</sup>

To evaluate the degree of graphitisation, the intensity ratio of the D peak and G peaks was calculated, where:

$$R = \frac{I_D}{I_G} \quad (21)$$

where  $R$  is the degree of graphitization of carbon materials,  $I_D$  is the intensity of the D peak,  $I_G$  is the intensity of the G peak. This ratio is widely used as a semi-quantitative indicator of structural disorder in carbon materials.<sup>83-85</sup>

In samples treated with sodium hydroxide, particularly ANCSH5, the D band intensity exceeded that of the G band, resulting in higher  $R$  values. In contrast, sulphuric acid-treated samples did not exhibit the same trend. Interestingly, higher  $R$  values, often associated with greater  $I_D$ , may also reflect an increased presence of aromatic ring structures and a partial reduction in certain types of carbon-related defects.<sup>79,85,86</sup> This structural evolution can enhance the formation of oxygen-containing functional groups on the material surface, thereby improving adsorption performance by increasing surface polarity and providing additional active sites for interaction with adsorbate molecules such as dyes. Overall, sodium hydroxide treatment promotes a higher degree of graphitisation compared to sulphuric acid treatment of the raw biomass.<sup>41,81</sup>

**3.2.4 Fourier Transform Infrared Spectroscopy (FTIR).** FTIR was employed to analyse the chemical transformations of functional groups in CPH following chemical activation with sodium hydroxide (NaOH, 0.1 M and 5 M) and sulphuric acid ( $H_2SO_4$ , 10 M) during the delignification process. As shown in Fig. 7a, the FTIR spectrum of untreated CPH reveals characteristic absorption bands of lignocellulosic biomass. A broad band near  $\sim 3400\text{ cm}^{-1}$  corresponds to O-H stretching vibrations associated with hydrogen bonding or adsorbed moisture, indicative of free hydroxyl groups on the surface.<sup>87</sup> The absorption at  $\sim 2894\text{ cm}^{-1}$  is attributed to C-H stretching of aliphatic,  $CH_2/-CH_3$  groups, linked to cellulose and hemicellulose structures.<sup>24</sup> The band at  $1722\text{ cm}^{-1}$  corresponds to C=O stretching in ester or carboxylic groups, likely originating from hemicellulose or lignin.<sup>20,87</sup> The signal at  $\sim 1600\text{ cm}^{-1}$  is attributed to aromatic C=C stretching or conjugated C=O groups within lignin, and may also reflect  $\pi-\pi$  interactions associated with emerging graphitised domains.<sup>5,55,89</sup> The peak at  $1426\text{ cm}^{-1}$  corresponds to aromatic skeletal C=C stretching,<sup>90</sup> while  $1314\text{ cm}^{-1}$  is assigned to in-plane C=C vibrations and symmetric C-H bending of methyl/methylene groups, common in lignin side chains and polysaccharide residues.<sup>88</sup> A strong band at  $1244\text{ cm}^{-1}$  corresponds to C-O-C ether bonds in lignin,<sup>21</sup> and the absorption at  $1028\text{ cm}^{-1}$  is assigned to C-O stretching of primary and secondary alcohols in cellulose and hemicellulose.<sup>5,21</sup> Finally, the band near  $590\text{ cm}^{-1}$  corresponds to out-of-plane C-H bending vibrations.<sup>62</sup>

In contrast, the FTIR spectra of NaOH-treated samples (Fig. 7b and c) show a progressive attenuation and

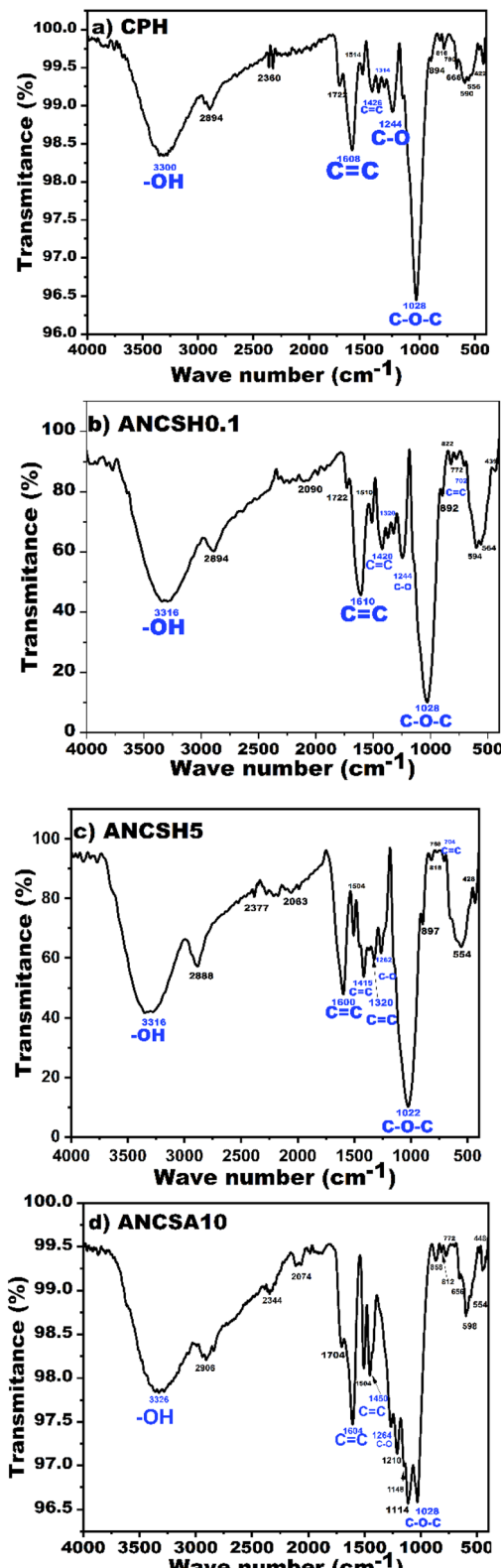


Fig. 7 FTIR spectra of (a) CPH, (b) ANCSH0.1, (c) ANCSH5, and (d) ANCSA10.

disappearance of the  $1722\text{ cm}^{-1}$  band, particularly in the ANCSH5 sample, indicating cleavage of ester linkages and effective removal of hemicellulose.<sup>24</sup> Similarly, the



disappearance of bands at  $1244\text{ cm}^{-1}$  and  $590\text{ cm}^{-1}$  confirms lignin degradation. This depolymerization process exposes hydroxyl and phenolic groups, thereby enhancing surface reactivity.<sup>23</sup> The alkaline treatment thus results in significant removal of recalcitrant fractions and increases cellulose accessibility, which is critical for adsorption efficiency.<sup>20</sup> Notably, new bands appeared at  $702\text{ cm}^{-1}$  (ANCSH0.1) and  $704\text{ cm}^{-1}$  (ANCSH5), associated with out-of-plane C-H bending in aromatic rings, suggesting the development of  $\pi$ - $\pi$  stacking interactions between carbon domains, possibly linked to partially graphitised structures.<sup>19,80</sup>

In the case of the acid-treated sample (Fig. 7d), the  $1722\text{ cm}^{-1}$  band was red-shifted to  $1704\text{ cm}^{-1}$ , indicating possible alterations in carbonyl environments due to partial conjugation. While the  $1244\text{ cm}^{-1}$  band (associated with either C-O-linkages in lignin) disappeared, suggesting partial lignin removal, the  $590\text{ cm}^{-1}$  band remained, indicating incomplete depolymerization of aromatic structures. In addition, intensified bands in the  $1210$ – $1114\text{ cm}^{-1}$  region were seen, associated with C-OH and C-O-C stretching, which are indicative of newly formed oxygen-containing acidic functionalities such as lactones, anhydrides, and phenols.<sup>24,55,89</sup> Notably, unlike the alkali-treated samples (ANCSH0.1 and ANCSH5), which exhibited new bands at  $702$  and  $704\text{ cm}^{-1}$ , respectively, attributed to  $\pi$ - $\pi$  stacking interactions, these bands were absent in the acid-treated ANCSA10. The disappearance of the  $1314\text{ cm}^{-1}$  band in ANCSA10 further supports the conclusion that sulphuric acid treatment was less effective for delignification and the development of aromatic carbon structures.

The band at  $1028\text{ cm}^{-1}$ , attributed to C-O stretching vibrations of primary and secondary alcohols in cellulose and hemicellulose, remained prominent after sulphuric acid treatment (ANCSA10), but showed a notable increase in intensity in the NaOH-treated samples (ANCSH0.1 and ANCSH5). This enhancement suggests a more effective removal of hemicellulose and lignin by the alkaline treatment, resulting in greater exposure of cellulose hydroxyl groups. These newly accessible polar functionalities can contribute significantly to adsorption performance by enabling electrostatic interactions and hydrogen bonding with cationic pollutants. Similar trends have been reported in other studies, where alkaline pretreatment led to a stronger  $1028\text{ cm}^{-1}$  signal due to increased cellulose accessibility.<sup>59,91,92</sup>

The more effective delignification achieved through NaOH treatment is attributed to enhanced cellulose exposure and the formation of surface oxygen-containing functional groups such as carbonyl, carboxyl, and hydroxyl groups. These functionalities are known to enhance adsorption performance through mechanisms such as electrostatic attraction, hydrogen bonding, and metal-ligand complexation.<sup>5</sup> According to previous studies, the nature and abundance of surface functional groups significantly influence the adsorption mechanism, with -COOH and -OH groups promoting the uptake of polar and ionic contaminants, including dyes and heavy metals.<sup>55,89</sup> Therefore, the applied chemical treatments effectively altered the surface chemistry of CPH, promoting the

generation of active sites and improving the material's affinity toward the target contaminant.

Although pure graphitic carbon exhibits minimal infrared activity due to its symmetrical and non-polar structure, partially graphitised domains formed during thermal activation of cellulose produce discernible FTIR bands. These include aromatic C=C stretching near  $1600$ – $1610\text{ cm}^{-1}$ , for all materials, as well as bands near  $1415$ – $1426$ ,  $1314$ – $1320$ , for CPH, ANCSH0.1, and ANCSH5; and  $702$ – $704\text{ cm}^{-1}$ . These latter bands are exclusively presented for ANCSH0.1 and ANCSH5, which are associated with  $\text{sp}^2$ -hybridised carbon structures and  $\pi$ - $\pi$  interactions, evidencing the alkaline treatment effect. These features reflect the evolution of oxygenated amorphous carbon networks derived from lignocellulosic precursors. Notably, lignin's inherent aromatic ring structures contribute to  $\pi$ -conjugated domains, facilitating  $\pi$ - $\pi$  stacking interactions with aromatic pollutants such as cationic methylene blue (MB<sup>+</sup>), which enhances adsorption efficiency, especially in alkaline-treated materials.<sup>24,40,41,89</sup>

FTIR analysis corroborated the structural changes identified by Raman spectroscopy and XRD. The presence of bands near  $1600\text{ cm}^{-1}$  (C=C stretching) and  $1220$ – $1260\text{ cm}^{-1}$  and  $1028\text{ cm}^{-1}$  (C-O stretching) confirms the formation of conjugated aromatic systems and oxygen-rich functionalities during chemical activation. These observations align with the D and G bands in Raman spectra, which signify the coexistence of disordered and graphitic carbon domains. Additionally, the broad peaks in the XRD patterns indicate the presence of amorphous or turbostratic carbon, supporting the formation of partially graphitised structures. Together, these spectroscopic and diffraction analyses demonstrate the successful conversion of CPH into a carbonaceous adsorbent with structural features favorable for  $\pi$ - $\pi$  interactions and electrostatic adsorption mechanisms.<sup>5,20,41,55</sup>

### 3.3 Adsorption studies

The adsorption performance of MB was evaluated using untreated CPH and chemically modified CPH powders (ANCSA10 and ANCSH5) under identical conditions:  $30\text{ }^\circ\text{C}$ , pH 7, and an initial dye concentration of  $5\text{ mg L}^{-1}$ . The removal efficiency followed the order: ANCSH5 > ANCSA10 > CPH. The untreated CPH achieved a removal efficiency of 24% ( $0.30\text{ mg g}^{-1}$ ), while ANCSA10 reached 44% ( $0.50\text{ mg g}^{-1}$ ). Remarkably, the alkaline-treated sample ANCSH5 exhibited a substantial improvement in MB removal (92%,  $1.155\text{ mg g}^{-1}$ ), highlighting the effectiveness of the NaOH activation in enhancing adsorption capacity.

Beyond adsorption efficiency, the sustainability of ANCSH5 is intrinsically linked to the valorisation of CPH, a locally abundant agro-waste with limited alternative applications. Its conversion into carbon prevents biomass accumulation in landfills, where uncontrolled biological decomposition generates methane (CH<sub>4</sub>), a potent greenhouse gas.<sup>22,38</sup> In addition, the synthesis employed here requires only sulphuric acid and sodium hydroxide pretreatments at moderate conditions, without the need for high-temperature furnaces, thus



minimizing energy consumption and the associated carbon footprint.<sup>39,47</sup> These attributes distinguish the present route from other biomass-based carbons and further from petroleum-derived ACs, whose production pathways involve fossil feedstocks with significant emissions of GreenHouse Gases (GHGs) and Volatile Organic Compounds (VOCs).<sup>15,77</sup> This highlights the “green” positioning of the proposed synthesis, which integrates waste reduction, low-energy processing, and circular economy principles.

This improvement may be attributed to the removal of organic compounds during the delignification process facilitated by alkaline treatment, which enhances the chelating ability of the adsorbent surface. Additionally, sodium hydroxide activation promotes a higher degree of graphitization compared to sulphuric acid treatment, leading to the formation of oxygen-containing functional groups. These modifications enhance surface polarity and create additional active sites, thereby enhancing the overall adsorption performance.

**3.3.1 Adsorption kinetics.** The adsorption kinetics of MB onto CPH, ANCSH5, and ANCSA10 are presented in Fig. 8. A rapid increase in adsorption capacity was seen within the first 60 min for CPH and ANCSH5, indicating high initial affinity towards MB. In contrast, ANCSA10 exhibited a slower uptake, reaching maximum adsorption at 120 min. Equilibrium was established at approximately 120 min for CPH and ANCSH5, while ANCSA10 achieved equilibrium after 150 min. The kinetic data were fitted to pseudo-first-order and pseudo-second-order models (Table 5). The pseudo-second-order model provided superior  $R^2$  and closer agreement between experimental and calculated adsorption capacities ( $q_e$ , exp and  $q_e$ , cal), indicating its better suitability for describing the system. These results suggest that the adsorption mechanism is governed predominantly by chemisorption processes, potentially involving electron sharing or exchange, such as surface complexation, ion exchange, or precipitation.<sup>41,93,94</sup>

**3.3.2 Isotherm experiments.** The nature of the adsorption process was determined using different adsorption isotherm models to establish the best-fitted isotherm. The adsorption

**Table 5** Kinetic parameters of MB on CPH, ANCSH5, and ANCSA10 obtained from the pseudo-first-order and pseudo-second-order models

Adsorbent	Pseudo-first-order kinetics		
	$k_1$ (min <sup>-1</sup> )	$q_e$ (mg g <sup>-1</sup> )	$R^2$
CPH	0.02513	0.21966	0.99826
ANCSH5	0.03045	0.71546	0.96173
ANCSA10	0.02825	0.99607	0.65892
Adsorbent	Pseudo-second-order kinetics		
	$k_2$ (g mg <sup>-1</sup> min <sup>-1</sup> )	$q_e$ (mg g <sup>-1</sup> )	$R^2$
CPH	0.12188	0.27490	0.99827
ANCSH5	0.11569	1.18085	0.99918
ANCSA10	0.00005	7.57070	0.98107

equilibrium data for MB on the three adsorbents (CPH, ANCSA10, and ANCSH5) were fitted to the Langmuir and the Freundlich models. The resulting parameters and  $R^2$  are summarised in Table 6.

The Langmuir model, which assumes monolayer adsorption onto a homogeneous surface with finite, identical sites, showed a strong correlation for ANCSH5 ( $R^2 = 0.9997$ ). This suggests that the adsorption onto ANCSH5 may involve more uniform active sites with higher energy affinity toward MB. In contrast, CPH and ANCSA10 yielded low Langmuir  $R^2$  values (0.53 and 0.14, respectively), indicating that the assumption of surface homogeneity does not hold for these materials.

The Freundlich model, which accounts for adsorption on heterogeneous surfaces, provided a better fit for CPH ( $R^2 = 0.85$ ) and ANCSH5 ( $R^2 = 0.9999$ ), while it still performed poorly for ANCSA10 ( $R^2 = 0.16$ ). These differences may be attributed to variations in surface functionalization and porosity induced by chemical treatment, as supported by FTIR and BET analyses.

As shown in Fig. 9, the experimental adsorption data were fitted using the non-linear forms of the Langmuir and the

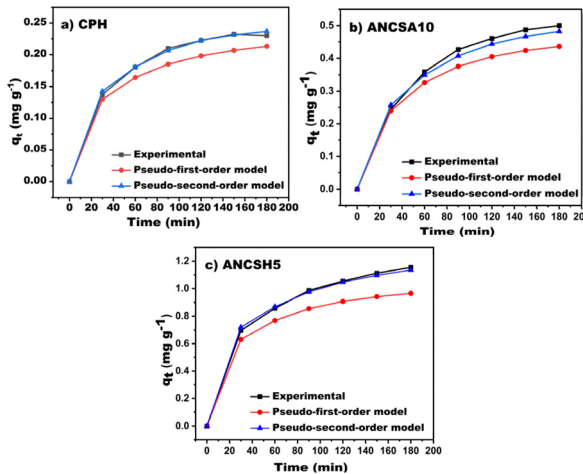


**Fig. 8** Adsorption kinetics of MB on (a) CPH, (b) ANCSA10, and (c) ANCSH5. Experimental conditions:  $C_0 = 5 \text{ mg L}^{-1}$ , pH 6,  $T = 30^\circ\text{C}$ .

**Table 6** Calculated equilibrium constants of MB on CPH, ANCSH5, and ANCSA10 obtained from the Langmuir and the Freundlich isotherm models

Adsorbent	Langmuir isotherm		
	$q_{\max}$ (mg g <sup>-1</sup> )	$K_L$ (L mg <sup>-1</sup> )	$R^2$
CPH	100.0000	0.002418	0.5291
ANCSH5	100.0000	0.024424	0.9997
ANCSA10	100.0000	0.007475	0.1416
Adsorbent	Freundlich isotherm		
	$K_F$ (mg <sup>1-1/n</sup> g <sup>-1</sup> L <sup>1/n</sup> )	$n$	$R^2$
CPH	0.000016	0.201033	0.8449
ANCSH5	2.377979	1.037309	0.9999
ANCSA10	0.356150	0.687208	0.1559



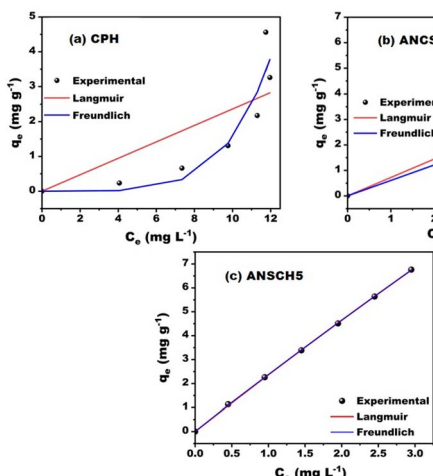


Fig. 9 Experimental adsorption isotherms ( $q_e$  vs.  $C_e$ ) of MB on (a) CPH, (b) ANCSA10, and (c) ANCSH5, fitted with Langmuir and Freundlich models.

Freundlich isotherm models. The results indicate an excellent fit for ANCSH5, moderate agreement for CPH, and poor conformity for ANCSA10, highlighting differences in surface characteristics and adsorption mechanisms among the adsorbents. In particular, CPH and ANCSA10 exhibited non-ideal and progressive adsorption behaviour. These deviations can be attributed to surface heterogeneity, low adsorbate–adsorbent affinity, and multilayer adsorption factors not fully captured by the monolayer assumption of the Langmuir model or the empirical approximation inherent to the Freundlich model. Importantly, although the equilibrium data showed deviations from classical isotherms, the adsorption process itself was effective, as evidenced by the high MB removal percentages and the excellent agreement of the kinetic data with the pseudo-second-order model. This reinforces the idea that adsorption performance should not be evaluated solely based on isotherm conformity, but also considering the dynamic interaction mechanisms and material-specific properties.

To further explore the equilibrium behaviour of MB adsorption onto the three adsorbents, extended isotherm models, including the Sips, Redlich–Peterson, Temkin, and Toth models, were applied. These models are useful for describing adsorption on heterogeneous surfaces, mixed adsorption mechanisms, or multilayer phenomena not captured by classical models. Fig. 10 shows the plots for the extended isotherm models (Redlich–Peterson, Sips, Temkin, and Toth), and the calculated isotherm constants are summarised in Table 7.

The Sips model, which combines elements of Langmuir and Freundlich, yielded excellent correlation for ANCSH5 ( $R^2 = 0.9997$ ), consistent with its previously seen near-monolayer behaviour with some degree of heterogeneity. For CPH, the model improved the fit moderately ( $R^2 = 0.84$ ), suggesting a surface with variable site energies. In contrast, ANCSA10 showed a limited correlation ( $R^2 = 0.29$ ), indicating that the model assumptions may not apply to its surface characteristics.

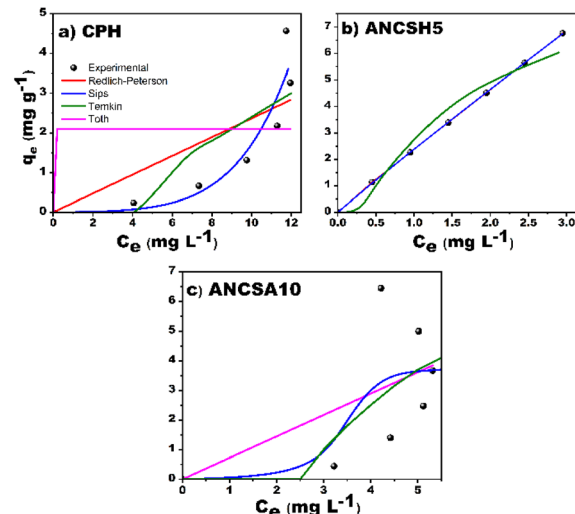


Fig. 10 Experimental adsorption isotherms ( $q_e$  vs.  $C_e$ ) of MB on (a) CPH, (b) ANCSH5, and (c) ANCSA10, fitted with extended isotherm models (Redlich–Peterson, Sips, Temkin, and Toth).

The Redlich–Peterson model, capable of bridging both Langmuir and Freundlich forms, also provided an exceptional fit for ANCSH5 ( $R^2 = 0.9999$ ). Its performance was slightly lower for CPH and poor for ANCSA10, again reflecting heterogeneity

Table 7 Calculated equilibrium constants of MB on CPH, ANCSH5, and ANCSA10 obtained from the Sips, Redlich–Peterson, Temkin, and Toth models

Adsorbent	Sips isotherm			
	$q_{\max}$ (mg g <sup>-1</sup> )	$K_s$ (L mg <sup>-1</sup> )	$n$	$R^2$
CPH	100.0000	0.0443	5.0955	0.8444
ANCSH5	100.0000	0.0248	1.0053	0.9997
ANCSA10	3.9212	0.2869	10.0000	0.2948
Redlich–Peterson isotherm				
Adsorbent	$K_R$ (L g <sup>-1</sup> )	$a_R$	$g$	$R^2$
CPH	18.0386	75.3073	0.0000	0.5357
ANCSH5	100.0000	41.0527	0.0368	0.9999
ANCSA10	42.2199	57.4525	0.0000	0.1431
Toth isotherm				
Adsorbent	$q_{\max}$ (mg g <sup>-1</sup> )	$K_T$ (L mg <sup>-1</sup> )	$t$	$R^2$
CPH	2.0345	14.4479	23.4162	0.0000
ANCSH5	100.0000	0.0241	1.0793	0.9998
ANCSA10	13.7814	0.0524	60.5573	0.1431
Temkin isotherm				
Adsorbent	$A$ (L g <sup>-1</sup> )	$B$	$R^2$	
CPH	0.2207	3.0693	0.6126	
ANCSH5	2.6914	2.9228	0.9306	
ANCSA10	0.4074	5.3564	0.1959	



Table 8  $R^2$  for all isotherm models

Adsorbent	Langmuir	Freundlich	Sips	Redlich-Peterson	Temkin	Toth
CPH	0.5291	0.8449	0.8444	0.5357	0.6126	0.0000
ANCSA10	0.1416	0.1559	0.2948	0.1431	0.1959	0.1431
ANCSH5	0.9997	0.9999	0.9997	0.9999	0.9306	0.9998

and non-ideal adsorption patterns. The Temkin model, which assumes a linear decrease in adsorption energy with coverage, showed moderate fits for CPH and ANCSH5, while underperforming for ANCSA10. This suggests that adsorbent-adsorbate interactions in these systems involve energetic heterogeneity or weak bonding effects. The Toth model, often used for highly heterogeneous systems, resulted in the best fit for ANCSH5 ( $R^2 \approx 1$ ) and improved fit for CPH compared to classical models. However, ANCSA10 again showed poor adjustment, highlighting its distinct and possibly multilayer or diffusion-limited adsorption mechanism.

ANCSH5 exhibited strong agreement with all models, particularly Redlich-Peterson and Toth, indicating a highly efficient and energetically accessible surface. The similarity in performance among classical and extended models for ANCSH5 suggests well-distributed active sites, moderate surface heterogeneity, and favorable interaction with the adsorbate. In contrast, ANCSA10 showed poor correlation across all models, indicating deviation from ideal or energetically uniform adsorption behaviour likely due to severe surface heterogeneity, inaccessible sites, or multilayer interactions. CPH showed moderate fits, with Sips and Temkin performing better.

In summary, the application of extended isotherm models supports the conclusion that ANCSH5 possesses a surface with high affinity and partially homogeneous active sites, whereas CPH shows heterogeneous behaviour with moderate adsorption energy. The poor fit of all models to ANCSA10 underscores the need for either customised models or hybrid approaches for

complex surfaces that incorporate kinetic or diffusional constraints.

**3.3.2.1 Model comparison based on coefficient of determination.** To systematically compare the performance of classical and extended isotherm models,  $R^2$  was calculated for each model and adsorbent (Table 8). This comparison reveals substantial differences in model performance depending on the material's surface chemistry and adsorption behaviour (Fig. 11).

Among the three adsorbents, ANCSH5 consistently exhibited the highest  $R^2$  values across all models, with nearly perfect fits for the Sips, Toth, and Redlich-Peterson models ( $R^2 > 0.99$ ). This indicates a well-defined and partially homogeneous adsorption mechanism, likely involving both high surface area and active functional groups enhanced by NaOH activation.

In contrast, CPH showed moderate fits, with the Freundlich and Sips models providing the best results ( $R^2 \approx 0.84$ ). The relatively low  $R^2$  values for Langmuir and Redlich-Peterson suggest that adsorption onto CPH occurs on a heterogeneous surface without saturation, likely due to limited availability or diversity of active sites.

ANCSA10 exhibited the lowest  $R^2$  values across nearly all models, including extended ones. This suggests a highly complex or non-ideal adsorption process, potentially involving multilayer formation, diffusion limitations, or weak interactions.

These findings reinforce the importance of applying a range of isotherm models, classical and extended, when characterizing novel adsorbents. Relying solely on Langmuir or Freundlich models may obscure underlying mechanistic differences, particularly in bio-based or structurally diverse materials, and reveal significant differences in adsorption capacity and surface affinity among the adsorbent materials.

**3.3.3 Thermodynamic studies.** Thermodynamic parameters were evaluated using the van't Hoff approach based on equilibrium constants ( $K_c = q_e/C_e$ ) obtained from isotherm data at different temperatures (25–45 °C). The standard Gibbs free energy ( $\Delta G^\circ$ ), enthalpy ( $\Delta H^\circ$ ), and entropy ( $\Delta S^\circ$ ) were calculated according to eqn (22–24):

$$\Delta G^\circ = -RT \ln K_c \quad (22)$$

$$\ln K_c = -\frac{\Delta H^\circ}{RT} + \frac{\Delta S^\circ}{R} \quad (23)$$

$$\Delta G^\circ = \Delta H^\circ - T\Delta S^\circ \quad (24)$$

Table 9 summarises the calculated thermodynamic parameters. Negative values of  $\Delta G^\circ$  across all tested temperatures confirm the spontaneous nature of MB adsorption onto

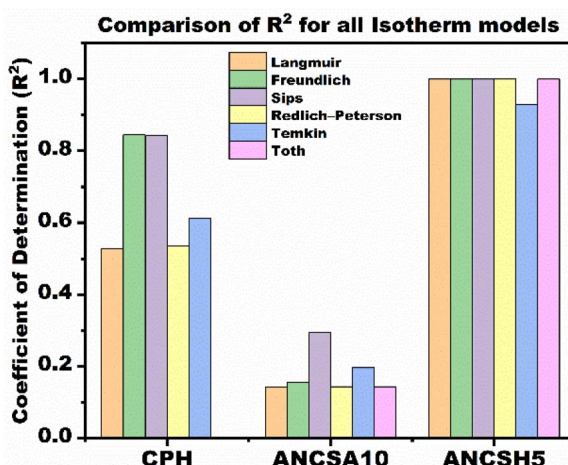


Fig. 11 Comparison of  $R^2$  obtained from classical and extended isotherm models for MB adsorption onto CPH, ANCSA10, and ANCSH5.



ANCSH5, consistent with observations reported for other biomass-derived adsorbents.<sup>9,57,95</sup> The positive  $\Delta H^\circ$  (25.0 kJ mol<sup>-1</sup>) indicates an endothermic process, while positive  $\Delta S^\circ$  values reflect increased randomness at the solid–liquid interface, in agreement with previous studies on dye adsorption involving natural adsorbents.<sup>64</sup> The magnitude of  $\Delta H^\circ$  suggests that the adsorption involves strong physicochemical interactions, consistent with electrostatic attraction, hydrogen bonding, and  $\pi$ – $\pi$  stacking mechanisms previously identified. These results corroborate the kinetic and isotherm analyses, demonstrating that MB adsorption on ANCSH5 is thermodynamically favorable, spontaneous, and enhanced at higher temperatures.<sup>9,57,95</sup>

**3.3.4 Isotherm modelling and effect of pH on adsorption behaviour.** The adsorption performance of CPH, ANCSH5, and ANCSA10 was evaluated through non-linear regression of classical (Langmuir and Freundlich) and extended (Redlich–Peterson, Sips, Toth, Temkin) isotherm models. Isotherm shapes, model parameters, and  $R^2$  revealed significant material-specific differences in adsorption mechanisms.

All experiments were conducted at pH 6, a condition near the slightly acidic regime, which can influence surface charge and adsorbate speciation. At this pH, functional groups such as hydroxyls and carboxyls on the adsorbent surface may be partially deprotonated, enhancing electrostatic attraction with cationic species or promoting hydrogen bonding. This effect is particularly favorable in materials with higher surface polarity and accessible acidic groups.

Among all tested adsorbents, ANCSH5 demonstrated the highest performance, with excellent agreement across all isotherm models ( $R^2 > 0.99$ ). The strong affinity seen at pH 6 indicates a surface rich in accessible functional groups whose ionization state promotes adsorption through electrostatic interactions and hydrogen bonding. These interactions are likely supported by the mildly acidic conditions, which optimise the charge distribution and polarity of the adsorbate–adsorbent system. This behaviour aligns with reports on functionalised bio-carbons, where pH-induced deprotonation increases the uptake of cationic dyes.<sup>96</sup>

CPH, while exhibiting moderate adsorption capacity, was best described by the Freundlich model ( $R^2 = 0.788$ ), suggesting adsorption on a heterogeneous surface with sites of varying energy. The lower  $R^2$  values obtained for the Langmuir and extended models indicate that adsorption at pH 6 deviates from ideal monolayer behaviour, potentially due to partial ionization of surface groups or weak adsorbate–adsorbent interactions under mildly acidic conditions. This limited affinity aligns with

prior studies on lignocellulosic adsorbents in similar pH environments.<sup>97,98</sup>

In contrast, ANCSA10 showed poor correlation with all isotherm models, including Sips and Toth ( $R^2 < 0.4$ ), indicating low adsorption capacity and inadequate model description at pH 6. This behaviour may result from surface deactivation, a low density of functional groups, or steric hindrance. The lack of improvement under acidic conditions suggests that its active sites are unresponsive to moderate pH shifts or that other mechanisms, such as deep microporosity, intraparticle diffusion, or non-electrostatic interactions, may dominate. Such deviations from equilibrium-based models have been previously reported for bio-based adsorbents with complex surface architectures.<sup>99</sup>

These findings highlight the crucial role of solution pH in regulating adsorption efficiency, particularly for bio-based adsorbents with heterogeneous surface chemistries. Under uniform pH 6 conditions, ANCSH5 exhibited superior performance, attributed to its surface functionality being well-aligned with mildly acidic environments. In contrast, CPH displayed a moderate adsorption response, while ANCSA10 remained largely unresponsive.

**3.3.4.1 Surface charge properties and  $pH_{PZC}$  determination.** The surface charge characteristics of the adsorbents were evaluated through the point of zero charge ( $pH_{PZC}$ ) determined by the pH-drift method, yielding values of 6.2 for ANCSH5 and 4.8 for ANCSA10 (Fig. 12). These differences have important implications for adsorption behaviour, as the  $pH_{PZC}$  defines the pH at which the surface switches from positive to negative charge. When the solution pH exceeds the  $pH_{PZC}$ , the surface becomes predominantly negatively charged, enhancing electrostatic attraction towards cationic dyes such as MB<sup>+</sup>; conversely, at pH values below the  $pH_{PZC}$ , electrostatic repulsion dominates.<sup>38,52</sup> Similar pH-dependent trends have been reported for biomass-derived carbons and low-cost adsorbents used for cationic dye removal.<sup>12,51,54,55</sup>

The acid dissociation constant ( $pK_a$ ) of MB is approximately 3.8, indicating that above this pH, the dye predominantly exists in its cationic form (MB<sup>+</sup>) in aqueous solution.<sup>100–102</sup> Consequently, under the experimental conditions employed in this work (pH 6–7), MB molecules are positively charged and readily

Table 9 Thermodynamic parameters for MB adsorption on ANCSH5

T (°C)	T (K)	$\Delta G^\circ$ (kJ mol <sup>-1</sup> )	$\Delta H^\circ$ (kJ mol <sup>-1</sup> )	$\Delta S^\circ$ (J mol <sup>-1</sup> K <sup>-1</sup> )
25	298.15	-4.76	25.0	99.8
35	308.15	-5.52	25.0	99.6
45	318.15	-6.28	25.0	99.1

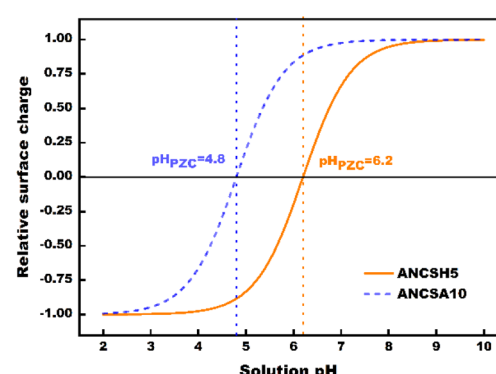


Fig. 12 Determination of the  $pH_{PZC}$  of ANCSH5 and ANCSA10 using the pH-drift method.



interact with negatively charged adsorbent surfaces. When the solution pH is equal to or higher than the  $\text{pH}_{\text{PZC}}$  (6.2 for ANCSH5 and 4.8 for ANCSA10), deprotonation of surface  $-\text{COOH}$  and  $-\text{OH}$  groups ( $-\text{COOH} \rightarrow -\text{COO}^-$ ;  $-\text{OH} \rightarrow -\text{O}^-$ ) generates a net negative charge, promoting strong electrostatic attraction with  $\text{MB}^+$ , in addition to hydrogen bonding and  $\pi-\pi$  stacking with aromatic domains on the carbon surface.

At near-neutral pH, ANCSH5 therefore exhibits superior adsorption capacity, consistent with its higher  $\text{pH}_{\text{PZC}}$  and greater availability of deprotonated oxygenated groups. Within the working pH window (6–7), the surface of ANCSH5 is partially deprotonated, exposing  $-\text{COO}^-$  and  $-\text{O}^-$  sites that enhance electrostatic interactions with  $\text{MB}^+$ , synergistically reinforced by  $\pi-\pi$  stacking between the dye's aromatic rings and the partially graphitised domains of the adsorbent.<sup>38,52,55</sup> In contrast, ANCSA10, with a lower  $\text{pH}_{\text{PZC}}$ , remains closer to a neutral or slightly positive surface state, limiting the availability of negatively charged sites and thus reducing electrostatic affinity for  $\text{MB}^+$ .<sup>12,26,51,54</sup> This interplay between the dye's  $\text{pK}_a$  and the adsorbent's  $\text{pH}_{\text{PZC}}$  is a decisive parameter governing the charge-controlled adsorption mechanism and explains the high adsorption efficiency observed at near-neutral pH.

Table 10 compares the maximum adsorption capacities of ACs derived from various lignocellulosic biomasses for MB removal, predicted by isotherm modelling. Although some biomass-based carbons report higher  $q_{\text{max}}$  values (e.g., coffee husk, pineapple residues), these capacities were typically obtained under extreme conditions, such as very high initial MB concentrations ( $\geq 400 \text{ mg L}^{-1}$ ) or excessive adsorbent dosages. By contrast, the NaOH-activated CPH (ANCSH5) synthesised in this work achieved a competitive  $q_{\text{max}}$  of  $100 \text{ mg g}^{-1}$  under more realistic operating conditions ( $C_0 = 5\text{--}30 \text{ mg L}^{-1}$ , pH 6, 35 °C,

dosage =  $4 \text{ g L}^{-1}$ ). This result is particularly relevant for practical wastewater treatment, where pollutant concentrations are moderate and the use of large adsorbent doses is economically unfeasible. Moreover, the integration of statistical optimisation *via* CCD-RSM adds a further competitive edge by ensuring that adsorption performance is guided by validated optimal conditions. The distinctive advantage of ANCSH5 compared with other biomass-derived carbons lies in the unique lignocellulosic composition of CPH, which is notably rich in hemicellulose. This facilitates extensive delignification during alkaline treatment and promotes the development of partially graphitised domains and a high density of oxygen-containing functional groups, as confirmed by Raman, XRD, and FTIR analyses. Unlike conventional precursors such as rice husk or coconut shell, where performance is largely governed by surface area, CPH-derived ANC combines enhanced graphitization with tailored surface chemistry. This synergy provides abundant active sites for electrostatic interactions, hydrogen bonding, and  $\pi-\pi$  stacking with MB molecules. Collectively, these features distinguish ANCSH5 as a competitive, sustainable, and industrially relevant adsorbent within the broader family of biomass-based carbons.

**3.3.4.2 Surface functionalization and interaction with  $\text{MB}^+$ .** The chemical activation processes applied to the adsorbents led to the incorporation of oxygen-containing functional groups on the carbon surface. These groups include carboxyl ( $-\text{COOH}$ ), hydroxyl ( $-\text{OH}$ ), and carbonyl ( $-\text{C}=\text{O}$ ) moieties, which are commonly formed through oxidation reactions during treatment with either acidic or alkaline agents. At pH 6, carboxylic groups tend to deprotonate, resulting in negatively charged carboxylate ( $-\text{COO}^-$ ) species, whereas hydroxyl and carbonyl groups contribute to surface polarity and hydrogen bonding

Table 10 Comparative  $q_{\text{max}}$  of biomass-derived carbons for MB removal, obtained from isotherm models<sup>a</sup>

Biomass precursor	Activation/treatment	$q_{\text{max}} (\text{mg g}^{-1})$	Conditions	Ref.
Coffee husk	Pyrolysis	416.68	MB $C_0$ range: 50–500 mg L $^{-1}$ ; pH: 7; T: 30 °C; adsorbent dosage: 1 g L $^{-1}$	5
Pineapple leaf powder	Untreated	281	MB $C_0$ range: 1.6–6.40 mg L $^{-1}$ ; pH: 7.5; T: 24 °C; adsorbent dosage: 0.3 g L $^{-1}$	51
Pineapple waste (leaves, stem, crown)	Pyrolysis	288.34	MB $C_0$ range: 5–400 mg L $^{-1}$ ; pH: 7; T: 30 °C; adsorbent dosage: 10 g L $^{-1}$	11
Watermelon rings	$\text{H}_2\text{SO}_4$	200	MB $C_0$ range: 50–400 mg L $^{-1}$ ; pH: 5.6; T: 30 °C; adsorbent dosage: 0.8 g L $^{-1}$	55
Sugarcane bagasse	Pyrolysis	113.01	MB $C_0$ range: 20–50 mg L $^{-1}$ ; pH: 7.4; T: 30 °C; adsorbent dosage: 0.6 g L $^{-1}$	3
Banana stem	Pyrolysis	101	MB $C_0$ range: 25–200 mg L $^{-1}$ ; pH: 7; T: 30 °C; adsorbent dosage: 3 g L $^{-1}$	54
Cocoa pod husk	NaOH	100	MB $C_0$ range: 5–30 mg L $^{-1}$ ; pH: 6; T: 35 °C; adsorbent dosage: 4 g L $^{-1}$	This study
Yellow passion-fruit peel	Untreated	44.7	MB $C_0$ range: 5–600 mg L $^{-1}$ ; pH: 8; T: 25 °C; adsorbent dosage: 10 g L $^{-1}$	57
Annona squamosa seed	$\text{H}_2\text{SO}_4$	25.91	MB $C_0$ range: 25–200 mg L $^{-1}$ ; pH: 6; T: 27 °C; adsorbent dosage: 4 g L $^{-1}$	96
Brazil nut shell	Untreated	7.81	MB $C_0$ range: 100–1500 mg L $^{-1}$ ; pH: 6.5; T: 30 °C; adsorbent dosage: 100 g L $^{-1}$	99

<sup>a</sup> MB  $C_0$ : MB initial concentration range.



capacity. Together, these functionalities enhance the overall hydrophilicity and facilitate electrostatic attraction with the  $\text{MB}^+$  molecules. This explains the improved adsorption performance seen in the NaOH-treated ANCSH5, in contrast to the  $\text{H}_2\text{SO}_4$ -activated ANCSA10, which likely retains a more protonated and less negatively charged surface under the same conditions.

FTIR analysis revealed that the band at  $1028\text{ cm}^{-1}$ , assigned to the C–O stretching of primary and secondary alcohols, became more intense following NaOH treatment, indicating a higher density of exposed hydroxyl groups on the surface. These –OH groups, primarily from cellulose, play a critical role in the adsorption mechanism by participating in hydrogen bonding and electrostatic interactions with the  $\text{MB}^+$  molecules. This is particularly relevant at pH 6, where partial deprotonation of hydroxyl and carboxyl groups enhances surface polarity and negative charge. The increased exposure of C–OH groups, especially in ANCSH5, correlates with the improved adsorption performance seen in kinetic and isotherm studies. Similar findings have been reported in the literature, where stronger C–O bands at  $\sim 1028\text{ cm}^{-1}$  were associated with improved adsorption properties due to enhanced accessibility of cellulose chains after alkaline pretreatment.<sup>59,91,92</sup>

At pH 6,  $\pi$ – $\pi$  stacking interactions are particularly relevant for the adsorption of  $\text{MB}^+$ , given its planar aromatic structure.<sup>24,41,55,89</sup> The FTIR spectra revealed stronger aromatic C=C bands for ANCSH5, indicating a higher density of conjugated  $\pi$ -systems capable of forming stable interactions with  $\text{MB}^+$ . These  $\pi$ – $\pi$  interactions provide an additional adsorption mechanism beyond electrostatic attraction, especially in cases where the surface charge is neutral or weakly positive (as in ANCSA10). In ANCSH5, both  $\pi$ – $\pi$  stacking and electrostatic forces act synergistically, leading to enhanced adsorption capacity and model fitting. Furthermore, this pH was selected to simulate mildly acidic wastewater conditions and to promote adsorption *via* electrostatic attraction, hydrogen bonding, and  $\pi$ – $\pi$  stacking.

Fig. 13 illustrates three primary interactions:

(1)  $\pi$ – $\pi$  stacking, involving the aromatic rings of  $\text{MB}^+$  and conjugated  $\pi$ -domains on the adsorbent surface.

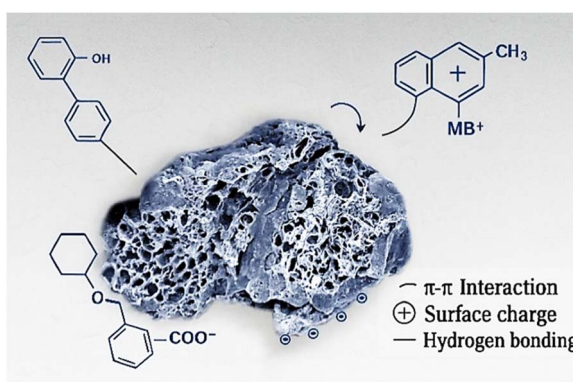


Fig. 13 Proposed adsorption mechanism of  $\text{MB}^+$  onto oxygen-functionalised carbon-based adsorbents at pH 6.

(2) Electrostatic attraction, driven by the deprotonation of carboxylic groups ( $-\text{COOH} \rightarrow -\text{COO}^-$ ) on the adsorbent at pH 6, which interacts with the positively charged  $\text{MB}^+$  molecules.

(3) Hydrogen bonding, between surface hydroxyl (–OH) or carbonyl (–C=O) groups and electronegative atoms of  $\text{MB}^+$ .

These combined interactions explain the strong affinity of  $\text{MB}^+$  toward materials like CPH and ANCSH5, where both surface polarity and negative charge enhance adsorption efficiency.

### 3.3.5 Experimental design CCD and optimisation studies.

Based on the CCD, the relationship between the process variables (temperature and pH) and the output responses, % MB removal and adsorption capacity, was modeled using a second-order polynomial equation. Table 11 presents both the experimental and predicted adsorption capacities derived from the design matrix. The incorporation of quadratic terms significantly enhanced the model's predictive capability, offering improved flexibility in identifying optimal operating conditions compared to the simpler linear interaction model. According to the RSM results, the following quadratic expression was derived.

$$\begin{aligned} \% \text{ Removal} = & 9.254 + 2.203T - 1.596 \text{ pH} + 0.191T \text{ pH} \\ & - 0.0338T^2 - 0.2052 \text{ pH}^2 \end{aligned} \quad (25)$$

$$\begin{aligned} \% q = & 0.0900 + 0.0283T + 0.0239 \text{ pH} + 0.0023T \text{ pH} - 0.0004T^2 \\ & - 0.0028 \text{ pH}^2 \end{aligned} \quad (26)$$

Tables 12 and 13 summarise the ANOVA results for the quadratic response surface models. The ANOVA for the sorption of MB onto ANCSH5 confirmed the overall statistical significance of the models, with  $F$ -values of 20.36 for % Removal and 20.69 for adsorption capacity ( $q$ , mg g<sup>-1</sup>). The corresponding  $p$ -values ( $<0.0001$ ) indicate that both regression models are highly significant. Moreover, the  $R^2$ , adjusted  $R^2$ , and predicted  $R^2$  values for both models exceeded 0.97, demonstrating excellent model fit, generalizability, and predictive reliability.

For % removal, the statistically significant model terms were  $X_1$  (temperature),  $X_2$  (pH),  $X_1^2$  (temperature<sup>2</sup>), and the interaction term  $X_1X_2$  (temperature  $\times$  pH). Both the linear and quadratic terms of temperature were highly significant ( $p < 0.001$ ), underscoring their critical influence on removal efficiency. The linear term for pH was also statistically significant ( $p < 0.01$ ), whereas its quadratic term was not ( $p > 0.4$ ). This suggests that pH affects the system primarily through linear behaviour and synergistic interaction with temperature, rather than exhibiting a pronounced curvilinear effect. The interaction term was statistically significant ( $p < 0.05$ ), confirming a synergistic influence between temperature and pH.

For  $q$  (mg g<sup>-1</sup>), a similar trend was seen. The significant terms were  $X_1$ ,  $X_1^2$ , and  $X_1X_2$ . Temperature remained the dominant factor, with both linear and quadratic terms showing strong statistical significance ( $p < 0.001$ ). The interaction term was also significant ( $p < 0.05$ ), whereas neither the linear nor the quadratic term of pH was. These findings reinforce the conclusion that adsorption capacity is primarily governed by



Table 11 Experimental and predicted responses (% removal and adsorption capacity,  $q$ ) obtained from the CCD matrix

Parameters	Response					
	(% Removal, $Y_1$ )			(Adsorption capacity ( $q$ ), mg g <sup>-1</sup> , $Y_2$ )		
Runs order	Temperature, $X_1$ (°C)	pH, $X_2$	Experimental	Predicted	Experimental	Predicted
1	35	2	59.51	60.70	0.74	0.76
2	35	6	90.70	87.23	1.13	1.09
3	65	2	35.83	36.88	0.45	0.46
4	65	6	89.92	86.31	1.12	1.07
5	29	4	68.82	69.96	0.86	0.87
6	71	4	51.32	52.65	0.64	0.66
7	50	1	47.90	45.87	0.60	0.57
8	50	7	98.66	100	1.23	1.28
9	50	4	75.13	76.20	0.94	0.95
10	50	4	78.12	76.20	0.98	0.95
11	50	4	76.14	76.20	0.95	0.95
12	50	4	75.20	76.20	0.94	0.95

Table 12 ANOVA for the % removal response surface quadratic model in the adsorption of MB by ANCSH5<sup>a</sup>

Source	Sum of squares	df	Mean square	F-value	p-value
Model	985.48	5	197.10	20.36	0.0011
$X_1$ -temperature	268.62	1	268.62	27.75	0.0019
$X_2$ -pH	226.05	1	226.05	23.35	0.0029
$X_1X_2$	131.10	1	131.10	13.54	0.0103
$X_1^2$	354.52	1	354.52	36.62	0.0009
$X_2^2$	5.19	1	5.19	0.54	0.4916
Residual	58.08	6	9.68		

<sup>a</sup>  $R^2 = 0.9852$ , adjusted  $R^2 = 0.9728$ , predicted  $R^2 = 0.9852$ ;  $p < 0.05$  indicates the model terms are significant;  $P < 0.01$  indicates the model terms are highly significant.

Table 13 ANOVA for  $q$  response surface model in the adsorption of MB by ANCSH5<sup>a</sup>

Source	Sum of squares	df	Mean square	F-value	p-value
Model	0.16	5	0.03	20.69	0.0010
$X_1$ -temperature	0.04	1	0.04	28.57	0.0018
$X_2$ -pH	0.04	1	0.04	23.78	0.0028
$X_1X_2$	0.02	1	0.02	12.95	0.0114
$X_1^2$	0.06	1	0.06	37.51	0.0009
$X_2^2$	0.00	1	0.00	0.65	0.4512
Residual	0.01	6	0.00		

<sup>a</sup>  $R^2 = 0.9850$ , adjusted  $R^2 = 0.9725$ , predicted  $R^2 = 0.9850$ ;  $p < 0.05$  indicates the model terms are significant;  $p < 0.01$  indicates the model terms are highly significant.

temperature, with pH exerting an indirect effect through interaction. The inclusion of interaction and quadratic terms is crucial for capturing surface curvature and enhancing model accuracy, particularly for complex adsorption behaviors.

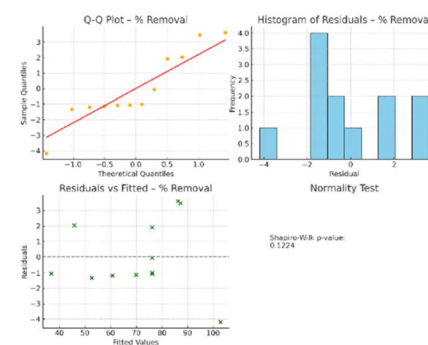
In summary, temperature emerged as the most influential variable in both models, while pH played a secondary but meaningful role through its interaction with temperature.

These results validate the use of quadratic models within RSM for process optimisation and provide a robust statistical foundation for predictive modelling in dye adsorption systems. The significant  $F$ - and  $R^2$ -values further support the inclusion of interaction and quadratic terms to capture the system's complexity.

Both response variables, % removal and adsorption capacity ( $q$ ), were strongly affected by temperature and its nonlinear behaviour. The temperature  $\times$  pH interaction contributed to refining the curvature of the response surface. Although pH alone was not statistically significant in the  $q$  model, and only marginally significant in the % removal model, its inclusion improved the overall model fit and predictive performance.

To evaluate the adequacy of the fitted quadratic models, residual diagnostics were conducted for both % removal and  $q$ . The assessment included Q-Q plots, histograms of residuals, residuals *versus* fitted values, and normality testing using the Shapiro-Wilk test.

For the % removal model (Fig. 14), the Q-Q plot showed that the residuals closely followed the theoretical normal distribution. The histogram of residuals appeared symmetric, and the

Fig. 14 Diagnostic plots for the quadratic model of % removal: Q-Q plot, histogram of residuals, residuals *versus* fitted values, and Shapiro-Wilk normality test ( $p = 0.1224$ ).

residuals *versus* fitted values displayed random scatter without discernible patterns, supporting the assumption of homoscedasticity. The Shapiro-Wilk test returned a *p*-value of 0.1224, exceeding the 0.05 threshold, thus confirming the normality of residuals.

Similarly, the diagnostic plots for the *q* model (Fig. 15) were consistent with the model assumptions. Residuals were normally distributed and randomly dispersed around zero across the range of fitted values. The Shapiro-Wilk test yielded a *p*-value of 0.1183, again supporting the normality assumption.

Collectively, these diagnostic results confirm that both models satisfy the key assumptions of regression analysis: normality, homoscedasticity, and independence of residuals. Meeting these criteria ensures the validity of hypothesis testing, confidence intervals, and optimisation results derived from the models. Accordingly, the response surfaces for both % removal and *q* can be interpreted with high statistical confidence.

Optimisation of the response surface models indicated that both % removal and *q* achieve their maximum predicted values under comparable operational conditions. For % removal, the optimal conditions were 49.6 °C and pH 6.0, yielding a predicted removal efficiency of 99.05%. Similarly, for *q*, the optimum was also found at 49.6 °C and pH 6.0, with a corresponding predicted adsorption capacity of 1.24 mg g<sup>-1</sup>.

The three-dimensional response surface plots, along with their corresponding contour diagrams, provide detailed visual insight into the interactive effects of temperature and pH on MB removal efficiency (% removal) and adsorption capacity (*q*, mg g<sup>-1</sup>). These graphical representations illustrate the curvature of the response surfaces and facilitate the identification of optimal operating conditions for both responses. The seen surface curvature and contour gradients emphasise the synergistic influence of temperature and pH, reinforcing their combined impact on system performance (Fig. 16 and 17).

In the response surface for % removal (Fig. 16), a pronounced curvature is seen, particularly along the temperature axis, confirming the strong nonlinear effect of

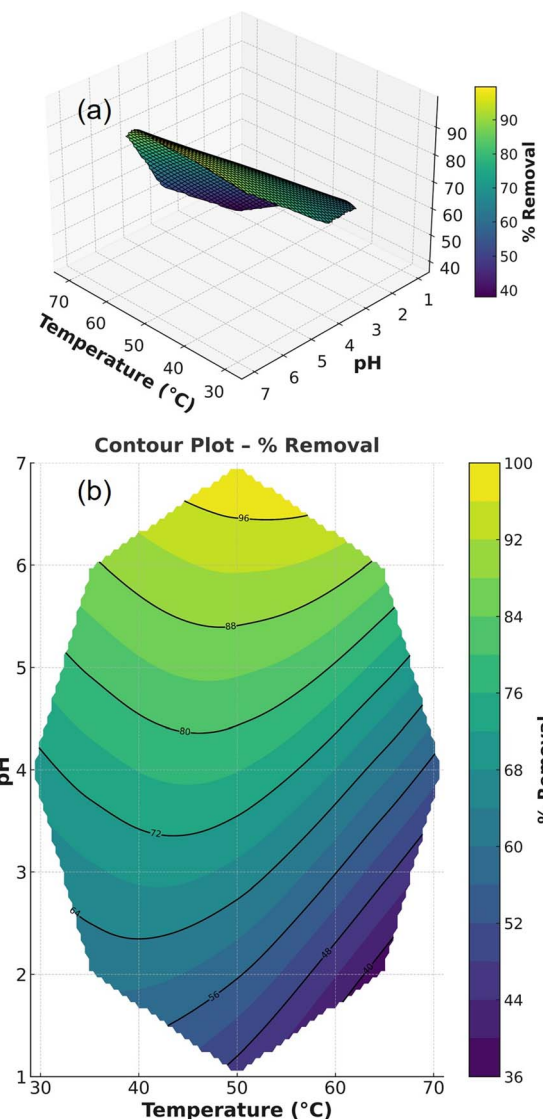


Fig. 16 Response surface 3D (a) and contour 2D (b) plots showing the interaction of temperature and pH on % MB removal.

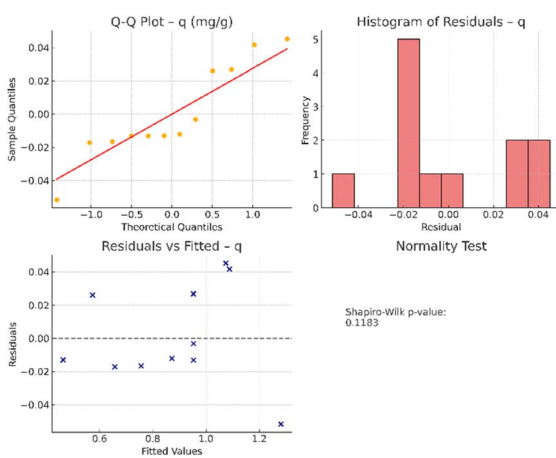


Fig. 15 Diagnostic plots for the quadratic model of *q*: Q-Q plot, histogram of residuals, residuals *vs.* fitted values, and Shapiro-Wilk normality test (*p* = 0.1224).

temperature. The response increases with temperature up to an optimal region (~49.6 °C), beyond which it gradually plateaus, likely due to the saturation of available adsorption sites. The influence of pH is more subtle but plays a role in fine-tuning the response, primarily through its interaction with temperature.

The corresponding contour plot for % removal reinforces these observations by delineating zones of high efficiency in the central region of the design space. A region of maximum removal efficiency (>95%) is centered around moderate to high temperatures (approximately 48–55 °C) and slightly acidic to neutral pH values (5.5–6.5). The presence of elongated, diagonally oriented elliptical contour lines highlights a significant interaction between temperature and pH, where small changes in pH at a given temperature can markedly affect the removal efficiency.

Similarly, the response surface plot for *q* exhibits a curved topography (Fig. 17), with a distinct maximum occurring at intermediate levels of both temperature and pH. Temperature



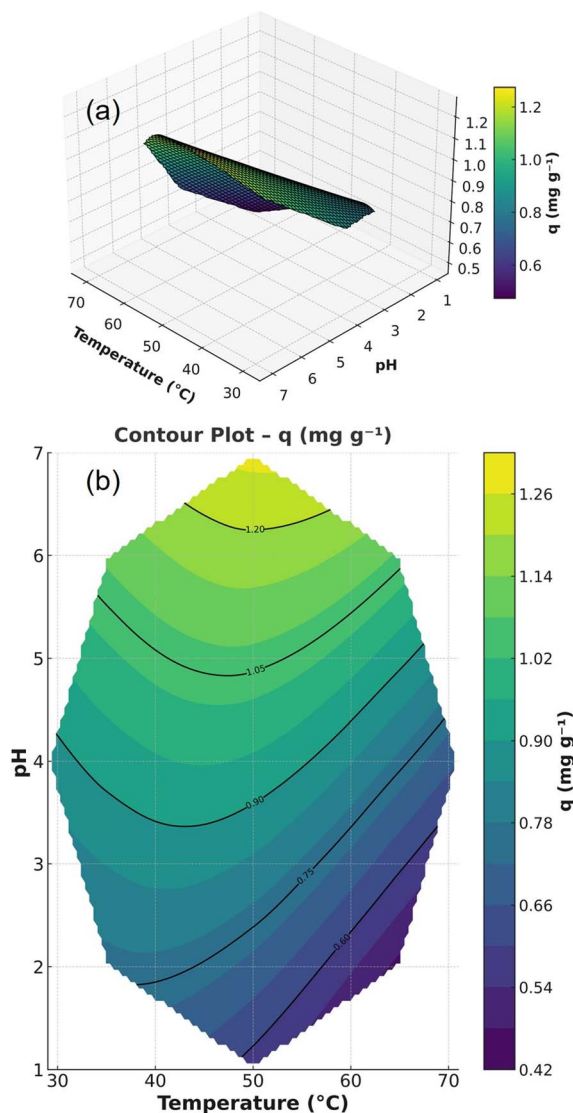


Fig. 17 Response surface 3D (a) and contour 2D (b) plots showing the interaction of temperature and pH on  $q$ .

again emerges as the dominant factor, while pH contributes to enhancing the response primarily through its synergistic interaction with temperature. The contour lines for  $q$  are more symmetrical and uniformly spaced, indicating a smoother gradient and suggesting broader operability within the optimal region.

The contour plot for  $q$  identifies a high-capacity adsorption zone ( $q > 1.1 \text{ mg g}^{-1}$ ) within a similar operational window, moderate temperatures (around 50 °C), and near-neutral pH values (6.0–6.5). In contrast to the % removal plot, the contour lines here are more concentric and evenly distributed, suggesting that  $q$  responds more uniformly to variations in either factor, with less pronounced interaction effects.

The overlap between high-response regions in both contour plots highlights a shared optimal range, demonstrating the feasibility of a unified set of operating conditions that simultaneously maximises % removal and  $q$ . These visual representations not only validate the predictive strength of the quadratic

regression models but also facilitate the direct identification of robust process windows, making them valuable tools for practical process control and scale-up.

Collectively, these graphical tools reinforce the statistical conclusions derived from the quadratic models and allow for intuitive visualization of factor interactions and response behaviour. The response surfaces confirm the adequacy of model fit and reveal the sensitivity of the process to changes in operating parameters, supporting robust and flexible process design.

Ultimately, the integration of these findings enables effective model-based optimisation and provides mechanistic insight into the adsorption behaviour under variable conditions. The developed models offer a reliable framework for predicting adsorption performance and serve as a foundation for advanced system design and scale-up in dye removal applications.

Although the ANOVA results for the quadratic model indicate that pH was not a statistically significant main factor ( $p > 0.05$ ), this does not imply that pH lacks influence within the adsorption system. Experimental evidence shows that at pH 6, the ANCSH5 adsorbent achieved higher % removal, which can be attributed to the physicochemical properties of its surface functional groups.

At this pH, the surface of ANCSH5 exposes a greater density of active binding sites, including deprotonated carboxyl groups and aromatic regions capable of  $\pi$ - $\pi$  stacking with  $\text{MB}^+$  molecules. These structural features enhance the adsorbent's affinity and capacity for dye uptake, particularly under slightly acidic to neutral conditions.

This mechanistic understanding aligns with the seen experimental enhancement in % removal at pH 6, despite the statistical model assigning low standalone significance to pH. The key lies in the interaction term: ANOVA revealed that the temperature  $\times$  pH interaction was statistically significant ( $p < 0.05$ ), indicating that the influence of pH becomes more pronounced when combined with thermal effects.

In contrast, other materials such as ANCSA10 and CPH did not exhibit similar performance at pH 6, likely due to differences in surface functionality and active site availability. This highlights the material-dependent nature of pH sensitivity in adsorption processes.

Thus, the apparent contradiction between statistical significance and experimental trends can be resolved. While pH may not exert a uniform linear influence across the design space, it plays a critical interactive role under specific conditions. The temperature remains the dominant variable, but pH significantly enhances adsorption performance when acting in synergy, particularly in materials like ANCSH5 with favorable surface chemistry.

## 4 Conclusions

This study demonstrated the green synthesis of ANC from CPH via acid and alkaline activation for MB removal. Among the prepared materials, ANCSH5 (NaOH, 5 M) exhibited the best performance due to extensive delignification, enhanced graphitization, and abundant oxygenated surface functionalities, as



confirmed by FTIR, SEM-EDX, BET, XRD, and Raman analyses. The improved surface polarity further promoted MB adsorption at pH 6 through electrostatic interactions, hydrogen bonding, and  $\pi$ - $\pi$  stacking. Adsorption followed pseudo-second-order kinetics, while equilibrium data were best fitted by the Freundlich, Sips, Toth, and Redlich-Peterson models ( $R^2 > 0.999$ ). Process optimisation using CCD-RSM identified optimal conditions (49.6 °C, pH 6.0), achieving 99.05% MB removal.

Importantly, ANCSH5 reached a competitive capacity (100 mg g<sup>-1</sup>, isotherm-derived) under realistic operating conditions ( $C_0 = 5$ –30 mg L<sup>-1</sup>, pH 6, 35 °C, dosage = 4 g L<sup>-1</sup>), unlike other biomass-derived carbons that report higher  $q_{\max}$  values only under extreme concentrations or excessive dosages. This distinctive performance arises from the hemicellulose-rich composition of CPH, which under alkaline activation promotes delignification, partial graphitization, and tailored surface chemistry. Together with validated statistical optimisation, these features establish CPH-derived ANC as a sustainable, low-cost, and industrially competitive adsorbent for dye remediation aligned with circular economy strategies. Overall, the synthesis route not only provides a high-performing adsorbent but also represents a greener alternative by coupling agro-waste valorisation with reduced energy and chemical demands, in contrast to conventional biomass- or fossil-based ACs.

This study did not include high-resolution electron microscopy (HRTEM) with particle-size analysis, density functional theory (DFT) calculations, or standardised ecotoxicity bioassays due to limited access to instrumentation. Nevertheless, the physicochemical characterisation and adsorption performance suggest that the materials may possess nanometric features, as supported by BET, SEM-EDX, XRD, Raman, and FTIR analyses, together with advanced isotherm and kinetic modelling. Additional high-resolution studies will be required to conclusively confirm their nanostructured nature. Future work will integrate HRTEM with quantitative particle sizing, DFT simulations of MB-surface interactions, and OECD-compliant ecotoxicity assays (e.g., *Daphnia magna* immobilisation and algal growth inhibition) to provide a more comprehensive understanding of structure–property relationships and environmental safety.

## Author contributions

Zenaida Guerra-Que: conceptualization, supervision, project administration, writing – review & editing, funding acquisition. Katia S. López-Margalli: methodology, investigation, data curation, writing – original draft. Juan Manuel Urrieta-Saltijeral: formal analysis, validation, software, visualization. Adib Abiu Silahua-Pavón: experimental design, response surface methodology analysis, resources. Héctor Martínez-García: characterisation (FTIR, SEM-EDX), data interpretation, writing – review & editing. Pedro García-Alamilla: Lignocellulosic analysis, Material preparation, Supervision. Gerardo E. Córdova-Pérez: XRD and raman analysis, instrumentation, technical support. Juan Carlos Arévalo-Pérez: SEM-EDX supervision, laboratory facilities, method validation. José Gilberto Torres-Torres: visualization, graphical abstract design, review, and critical revisions.

## Conflicts of interest

The authors declare no conflicts of interest.

## Data availability

The data supporting the findings of this study are available within the article. Additional datasets generated and analyzed during the current study are available from the corresponding author upon request.

## Acknowledgements

The authors gratefully acknowledge the support from Tecnológico Nacional de México – Instituto Tecnológico de Villahermosa and Universidad Juárez Autónoma de Tabasco. Special thanks are extended to the laboratory staff for their assistance with instrumental analysis.

## References

- 1 R. Gusain, N. Kumar and S. S. Ray, Recent advances in carbon nanomaterial-based adsorbents for water purification, *Coord. Chem. Rev.*, 2020, **405**, 213111.
- 2 C. I. Orozco, M. S. Freire, D. Gomez-Diaz and J. Gonzalez-Alvarez, Removal of copper from aqueous solutions by biosorption onto pine sawdust, *Sustainable Chem. Pharm.*, 2023, **32**, 101016.
- 3 S. Biswas, S. S. Mohapatra, U. Kumari, B. C. Meikap and T. K. Sen, Batch and continuous closed circuit semi-fluidized bed operation: Removal of MB dye using sugarcane bagasse biochar and alginate composite adsorbents, *J. Environ. Chem. Eng.*, 2020, **8**(1), 103637.
- 4 J. O. Ighalo and A. G. Adeniyi, Adsorption of pollutants by plant bark derived adsorbents: an empirical review, *J. Water Process Eng.*, 2020, **35**, 101228.
- 5 T. H. Tran, A. H. Le, T. H. Pham, D. T. Nguyen, S. W. Chang, W. J. Chung, *et al.*, Adsorption isotherms and kinetic modeling of methylene blue dye onto a carbonaceous hydrochar adsorbent derived from coffee husk waste, *Sci. Total Environ.*, 2020, **725**, 138325.
- 6 S. Wang, X. Chen, L. Fang, H. Gao, M. Han, X. Chen, *et al.*, Double heterojunction CQDs/CeO<sub>2</sub>/BaFe<sub>12</sub>O<sub>19</sub> magnetic separation photocatalysts: Construction, structural characterization, dye and POPs removal, and the interrelationships between magnetism and photocatalysis, *Nucl. Anal.*, 2022, **1**(3), 100026.
- 7 S. Naghdi, M. M. Shahrestani, M. Zendehbad, H. Djahaniani, H. Kazemian and D. Eder, Recent advances in application of metal-organic frameworks (MOFs) as adsorbent and catalyst in removal of persistent organic pollutants (POPs), *J. Hazard. Mater.*, 2023, **442**, 130127.
- 8 M. Sharkey, S. Harrad, M. A. E. Abdallah, D. S. Drage and H. Berresheim, Phasing-out of legacy brominated flame retardants: The UNEP Stockholm Convention and other



legislative action worldwide, *Environ. Int.*, 2020, **144**, 106041.

9 F. Dhaouadi, L. Sellaoui, G. L. Dotto, A. Bonilla-Petriciolet, A. Erto and A. B. Lamine, Adsorption of methylene blue on comminuted raw avocado seeds: Interpretation of the effect of salts via physical monolayer model, *J. Mol. Liq.*, 2020, **305**, 112815.

10 Y. Zhou, L. Zhang and Z. Cheng, Removal of organic pollutants from aqueous solution using agricultural wastes: a review, *J. Mol. Liq.*, 2015, **212**, 739–762.

11 M. N. Mahamad, M. A. A. Zaini and Z. A. Zakaria, Preparation and characterization of activated carbon from pineapple waste biomass for dye removal, *Int. Biodeterior. Biodegrad.*, 2015, **102**, 274–280.

12 P. M. Thabede, N. D. Shooto and E. B. Naidoo, Removal of methylene blue dye and lead ions from aqueous solution using activated carbon from black cumin seeds, *S. Afr. J. Chem. Eng.*, 2020, **33**(1), 39–50.

13 K. A. Adegoke and O. S. Bello, Dye sequestration using agricultural wastes as adsorbents, *Water Resour. Ind.*, 2015, **12**, 8–24.

14 N. B. Singh, G. Nagpal and S. Agrawal, Water purification by using adsorbents: a review, *Environ. Technol. Innovation*, 2018, **11**, 187–240.

15 S. Husien, R. M. El-taweel, A. I. Salim, I. S. Fahim, L. A. Said and A. G. Radwan, Review of activated carbon adsorbent material for textile dyes removal: Preparation, and modelling, *Curr. Res. Green Sustainable Chem.*, 2022, **5**, 100325.

16 V. E. Akpan, D. O. Omole and D. E. Bassey, Assessing the public perceptions of treated wastewater reuse: opportunities and implications for urban communities in developing countries, *Heliyon*, 2020, **6**(10), e05260.

17 W. Artifon, K. Cesca, C. J. de Andrade, A. A. U. de Souza and D. de Oliveira, Dyestuffs from textile industry wastewaters: Trends and gaps in the use of bioflocculants, *Process Biochem.*, 2021, **111**, 181–190.

18 A. I. Akinjokun, L. F. Petrik, A. O. Ogunfowokan, J. Ajao and T. V. Ojumu, Isolation and characterization of nanocrystalline cellulose from cocoa pod husk (CPH) biomass wastes, *Heliyon*, 2021, **7**(4), e06880.

19 N. G. Akam, B. S. Diboma, J. Z. Mfomo, B. Ndiwe, B. V. Bôt and A. B. Biwolé, Physicochemical characterization of briquette fuel produced from cocoa pod husk case of Cameroon, *Energy Rep.*, 2024, **11**, 1580–1589.

20 L. Y. Ouattara, E. K. A. Kouassi, D. Soro, K. B. Yao, G. D. Fanou, A. P. Drogui, *et al.*, Optimization of thermochemical hydrolysis of potassium hydroxide-delignified Cocoa (*Theobroma cacao* L) pod husks under low combined severity factors (CSF) conditions, *Sci. Afr.*, 2023, **22**, e01908.

21 L. F. Zambrano-Mite, Y. Villasana, M. L. Bejarano, C. Luciani, D. Niebieskikwiat, W. Alvarez, D. F. Cueva, D. Aguilera-Pesantes and L. M. Orejuela-Escobar, Optimization of microfibrillated cellulose isolation from cocoa pod husk via mild oxalic acid hydrolysis: A response surface methodology approach, *Heliyon*, 2023, **9**(6), e17258.

22 S. O. Dahunsi, C. O. Osueke, T. M. A. Olayanju and A. I. Lawal, Co-digestion of *Theobroma cacao* (Cocoa) pod husk and poultry manure for energy generation: Effects of pretreatment methods, *Bioresour. Technol.*, 2019, **283**, 229–241.

23 M. D. G. De Luna, W. Budianta, K. K. P. Rivera and R. O. Arazo, Removal of sodium diclofenac from aqueous solution by adsorbents derived from cocoa pod husks, *J. Environ. Chem. Eng.*, 2017, **5**(2), 1465–1474.

24 F. Ling Pua, M. S. Sajab, C. H. Chia, S. Zakaria, I. A. Rahman and M. S. Salit, Alkaline-treated cocoa pod husk as adsorbent for removing methylene blue from aqueous solutions, *J. Environ. Chem. Eng.*, 2013, **1**(3), 460–465.

25 MAPO. Mexican Agriculture Public Organization. From Mexico to the world: Cocoa. [Internet]. 2022 [cited 2025 Jul 28]. Available from: <https://www.gob.mx/agricultura/articulos/de-mexico-para-el-mundo-cacao>.

26 S. Benkaddour, R. Slimani, H. Hiyane, I. El Ouahabi, I. Hachoumi, S. El Antri, *et al.*, Removal of reactive yellow 145 by adsorption onto treated watermelon seeds: kinetic and isotherm studies, *Sustainable Chem. Pharm.*, 2018, **10**, 16–21.

27 P. N. Fotsing, N. Bouazizi, E. D. Woumfo, N. Mofaddel, F. Le Derf and J. Vieillard, Investigation of chromate and nitrate removal by adsorption at the surface of an amine-modified cocoa shell adsorbent, *J. Environ. Chem. Eng.*, 2021, **9**(1), 104618.

28 L. L. Díaz-Muñoz, A. Bonilla-Petriciolet, H. E. Reynel-Ávila and D. I. Mendoza-Castillo, Sorption of heavy metal ions from aqueous solution using acid-treated avocado kernel seeds and its FTIR spectroscopy characterization, *J. Mol. Liq.*, 2016, **215**, 555–564.

29 K. Rasoulpoor, A. P. Marjani and E. Nozad, Competitive chemisorption and physisorption processes of a walnut shell based semi-IPN bio-composite adsorbent for lead ion removal from water: Equilibrium, Kinetic and Thermodynamic studies, *Environ. Technol. Innovation*, 2020, **20**, 101133.

30 C. E. Onu, B. N. Ekwueme, P. E. Ohale, C. P. Onu, C. O. Asadu, C. C. Obi, *et al.*, Decolourization of bromocresol green dye solution by acid functionalized rice husk: artificial intelligence modeling, GA optimization, and adsorption studies, *J. Hazard. Mater. Adv.*, 2023, **9**, 100224.

31 F. A. Pavan, Y. Gushikem, A. C. Mazzocato, S. L. P. Dias and E. C. Lima, Statistical design of experiments as a tool for optimizing the batch conditions to methylene blue biosorption on yellow passion fruit and mandarin peels, *Dyes Pigm.*, 2007, **72**(2), 256–266.

32 İ. Şentürk and M. Alzein, Adsorptive removal of basic blue 41 using pistachio shell adsorbent-Performance in batch and column system, *Sustainable Chem. Pharm.*, 2020, **16**, 100254.

33 C. J. Entia, M. Cainoy, C. M. Bahian, N. R. Salon, R. J. Labadan and R. Arazo, Removal of Rhodamine-B dye



from aqueous solutions using alkaline-modified activated carbon from cocoa pod husk, *Bull. Environ. Contam. Toxicol.*, 2024, **113**(1), 33, DOI: [10.1007/s00128-024-03948-0](https://doi.org/10.1007/s00128-024-03948-0).

34 I. A. Kuti, J. J. Musa, B. A. Adabembe, F. U. Adigun, O. E. Abdulmuizz and G. B. Kayode, Production, characterisation and application of activated carbon from cocoa pod husk and banana peel using chemical impregnation (sulphuric acid) for soil amendment, *Int. Agric. Eng. J.*, 2025, **27**, 60–69.

35 M. G. Petrov, O. V. Startsev, M. P. Lebedev, M. M. Kopyrin and V. G. Salnikov, Strength characteristics of carbon fiber reinforced plastic in shear and cyclic extension-compression after 7 years of climate exposure, *C-J Carbon Res.*, 2024, **21**, 19–31, DOI: [10.37256/ujcr.2120244131](https://doi.org/10.37256/ujcr.2120244131).

36 W. T. Tsai, C. H. Hsu, Y. Q. Lin, C. H. Tsai, W. S. Chen and Y. T. Chang, Enhancing the pore properties and adsorption performance of cocoa pod husk (CPH)-derived biochars via post-acid treatment, *Processes*, 2020, **8**(2), 144.

37 J. N. Putro, F. E. Soetaredjo, S. Y. Lin, Y. H. Ju and S. Ismadji, Pretreatment and conversion of lignocellulosic biomass into valuable chemicals, *RSC Adv.*, 2016, **6**(52), 46834–46852.

38 Y. Dai, Q. Sun, W. Wang, L. Lu, M. Liu, J. Li, *et al.*, Utilizations of agricultural waste as adsorbent for the removal of contaminants: A review, *Chemosphere*, 2018, **211**, 235–253.

39 G. Velvizhi, C. Goswami, N. P. Shetti, E. Ahmad, K. K. Pant and T. M. Aminabhavi, Valorisation of lignocellulosic biomass to value-added products: Paving the pathway towards low-carbon footprint, *Fuel*, 2022, **313**, 122678.

40 N. Kumar, A. Pandey and Y. C. Sharma, A review on sustainable mesoporous activated carbon as adsorbent for efficient removal of hazardous dyes from industrial wastewater, *J. Water Process Eng.*, 2023, **54**, 104054.

41 Y. S. Reddy, N. K. Rotte, B. K. Sudhakar, N. R. Chand, R. J. Naik, S. Mandal, *et al.*, Biomass-derived sustainable mesoporous activated carbon as an efficient and recyclable adsorbent for the adsorption of hazardous dyes, *Hybrid Adv.*, 2024, **6**, 100218.

42 W. Horwitz and G. Latimer, *AOAC Official Methods of Analysis of AOAC International*, AOAC International, Gaithersburg (MD), 18th ed, 2005.

43 A. Sluiter, B. Hames, R. Ruiz, C. Scarlata, J. Sluiter, D. Templeton and D. Crocker, *Determination of Structural Carbohydrates and Lignin in Biomass. Laboratory Analytical Procedure (LAP)*, National Renewable Energy Laboratory (NREL), Golden, CO (USA), 2012, Report No.: NREL/TP-510-42618.

44 G. Selvaraju and N. K. A. Bakar, Production of a new industrially viable green-activated carbon from *Artocarpus integer* fruit processing waste and evaluation of its chemical, morphological and adsorption properties, *J. Cleaner Prod.*, 2017, **141**, 989–999, DOI: [10.1016/j.jclepro.2016.09.145](https://doi.org/10.1016/j.jclepro.2016.09.145).

45 S. Li, S. Su, S. Liu, C. Yang and Q. Lu, Fast pyrolysis of biomass in free-fall reactor for hydrogen-rich gas, *Fuel* *Process. Technol.*, 2004, **85**, 1201–1211, DOI: [10.1016/j.fuproc.2003.12.003](https://doi.org/10.1016/j.fuproc.2003.12.003).

46 M. P. Elizalde-González and V. Hernández-Montoya, Guava seed as an adsorbent and as a precursor of carbon for the adsorption of acid dyes, *Bioresour. Technol.*, 2009, **100**(7), 2111–2117.

47 N. M. Nor, L. C. Lau, K. T. Lee and A. R. Mohamed, Synthesis of activated carbon from lignocellulosic biomass and its applications in air pollution control—a review, *J. Environ. Chem. Eng.*, 2013, **1**(4), 658–666.

48 A. C. Ferrari and J. Robertson, Interpretation of Raman spectra of disordered and amorphous carbon, *Phys. Rev. B*, 2000, **61**(20), 14095.

49 M. Sevilla and A. B. Fuertes, The production of carbon materials by hydrothermal carbonization of cellulose, *Carbon (N Y)*, 2009, **47**(9), 2281–2289.

50 Z. Li, L. Deng, I. A. Kinloch and R. J. Young, Raman spectroscopy of carbon materials and their composites: Graphene, nanotubes and fibres, *Prog. Mater. Sci.*, 2023, **135**, 101089.

51 C. H. Weng, Y. T. Lin and T. W. Tzeng, Removal of methylene blue from aqueous solution by adsorption onto pineapple leaf powder, *J. Hazard. Mater.*, 2009, **170**(1), 417–424.

52 X. Tan, Y. Liu, G. Zeng, X. Wang, X. Hu, Y. Gu, *et al.*, Application of biochar for the removal of pollutants from aqueous solutions, *Chemosphere*, 2015, **125**, 70–85.

53 M. Mehmandoust, G. Li and N. Erk, Biomass-derived carbon materials as an emerging platform for advanced electrochemical sensors: recent advances and future perspectives, *Ind. Eng. Chem. Res.*, 2022, **62**(11), 4628–4635.

54 E. Misran, O. Bani, E. M. Situmeang and A. S. Purba, Banana stem based activated carbon as a low-cost adsorbent for methylene blue removal: Isotherm, kinetics, and reusability, *Alexandria Eng. J.*, 2022, **61**(3), 1946–1955.

55 A. H. Jawad, R. Razuan, J. N. Appaturi and L. D. Wilson, Adsorption and mechanism study for methylene blue dye removal with carbonized watermelon (*Citrullus lanatus*) rind prepared via one-step liquid phase  $H_2SO_4$  activation, *Surf. Interfaces*, 2019, **16**, 76–84.

56 T. M. Dao and T. Le Luu, Synthesis of activated carbon from macadamia nutshells activated by  $H_2SO_4$  and  $K_2CO_3$  for methylene blue removal in water, *Bioresour. Technol. Rep.*, 2020, **12**, 100583.

57 F. A. Pavan, E. C. Lima, S. L. P. Dias and A. C. Mazzocato, Methylene blue biosorption from aqueous solutions by yellow passion fruit waste, *J. Hazard. Mater.*, 2008, **150**(3), 703–712.

58 J. Lladó, F. López, J. M. Rossell, C. Lao-Luque, R. R. Gil, E. Fuente, *et al.*, Multivariate analysis of pharmaceutical pollutants adsorption in aqueous media with tailored waste-based carbonaceous adsorbent materials and commercial activated carbons, *Sustainable Chem. Pharm.*, 2024, **38**, 101453.

59 L. S. de Souza, A. M. Pereira, S. Farias MA dos, R. L. e Oliveira, D. Junior and J. N. N. Quaresma, Valorization of Andiroba (*Carapa guianensis* Aubl.) residues through



optimization of alkaline pretreatment to obtain fermentable sugars, *Bioresources*, 2020, **15**(1), 894.

60 R. A. K. Rao and U. Khan, Adsorption of Ni (II) on alkali treated pineapple residue (*Ananas comosus* L.): Batch and column studies, *Groundw. Sustain. Dev.*, 2017, **5**, 244–252.

61 J. Rajendran, A. Panneerselvam, S. Ramasamy and P. Palanisamy, Methylene blue and methyl orange removal from wastewater by magnetic adsorbent based on activated carbon synthesised from watermelon shell, *Desalin. Water Treat.*, 2024, **317**, 100040.

62 T. K. O. Le, S. Jung, T. H. Pham and T. Kim, Highly porous biomass-derived graphene-based carbons for removal of phenol from wastewater, *Colloids Surf., A*, 2024, **699**, 134588.

63 E. A. Khan and T. A. Khan, Adsorption of methyl red on activated carbon derived from custard apple (*Annona squamosa*) fruit shell: equilibrium isotherm and kinetic studies, *J. Mol. Liq.*, 2018, **249**, 1195–1211.

64 I. Ghosh, S. Kar, T. Chatterjee, N. Bar and S. K. Das, Adsorptive removal of Safranin-O dye from aqueous medium using coconut coir and its acid-treated forms: adsorption study, scale-up design, MPR and GA-ANN modeling, *Sustainable Chem. Pharm.*, 2021, **19**, 100374.

65 L. A. Araujo, C. O. Bezerra, L. F. Cusioli, M. T. Rodríguez, R. G. Gomes and R. Bergamasco, Diclofenac adsorption using a low-cost adsorbent derived from *Guazuma ulmifolia* Lam. fruit via chemical and thermal treatment, *J. Environ. Chem. Eng.*, 2021, **9**(6), 106629.

66 V. G. Georgieva, L. Gonsalvesh and M. P. Tavlieva, Thermodynamics and kinetics of the removal of nickel (II) ions from aqueous solutions by biochar adsorbent made from agro-waste walnut shells, *J. Mol. Liq.*, 2020, **312**, 112788.

67 R. Minjares-Fuentes, A. Femenia, M. C. Garau, M. G. Candelas-Cadillo, S. Simal and C. Rosselló, Ultrasound-assisted extraction of hemicelluloses from grape pomace using response surface methodology, *Carbohydr. Polym.*, 2016, **138**, 180–191.

68 P. Kowalczyk, B. Ligas, D. Skrzypczak, K. Mikula, G. Izidorczyk, A. Witek-Krowiak, *et al.*, Biosorption as a method of biowaste valorization to feed additives: RSM optimization, *Environ. Pollut.*, 2021, **268**, 115937.

69 N. T. Abdel-Ghani, G. A. El-Chaghaby, E. S. A. Rawash and E. C. Lima, Magnetic activated carbon nanocomposite from *Nigella sativa* L. waste (MNSA) for the removal of Coomassie brilliant blue dye from aqueous solution: Statistical design of experiments for optimization of the adsorption conditions, *J. Adv. Res.*, 2019, **17**, 55–63.

70 A. Elhalil, H. Tounsiadi, R. Elmoubarki, F. Z. Mahjoubi, M. Farnane, M. Sadiq, *et al.*, Factorial experimental design for the optimization of catalytic degradation of malachite green dye in aqueous solution by Fenton process, *Water Resour. Ind.*, 2016, **15**, 41–48.

71 S. Farooq, A. Saeed, M. Sharif, J. Hussain, F. Mabood and M. Iftekhar, Process optimization studies of crystal violet dye adsorption onto novel, mixed metal  $\text{Ni}_{0.5}\text{Co}_{0.5}\text{Fe}_2\text{O}_4$  ferrospinel nanoparticles using factorial design, *J. Water Process Eng.*, 2017, **16**, 132–141.

72 M. A. Aly-Eldeen, A. A. M. El-Sayed, D. M. S. A. Salem and G. M. El Zokm, The uptake of Eriochrome Black T dye from aqueous solutions utilizing waste activated sludge: Adsorption process optimization using factorial design, *Egypt. J. Aquat. Res.*, 2018, **44**(3), 179–186.

73 J. Ponce, S. A. J. G. da, L. N. dos Santos, M. K. Bulla, B. C. B. Barros, S. L. Favaro, *et al.*, Alkali pretreated sugarcane bagasse, rice husk and corn husk wastes as lignocellulosic biosorbents for dyes, *Carbohydr. Polym. Technol. Appl.*, 2021, **2**, 100061.

74 M. Mergbi, M. G. Galloni, D. Aboagye, E. Elimian, P. Su, B. M. Ikram, *et al.*, Valorization of lignocellulosic biomass into sustainable materials for adsorption and photocatalytic applications in water and air remediation, *Environ. Sci. Pollut. Res.*, 2023, **30**(30), 74544–74574.

75 S. R. Mousavi-Qeydari, A. Samimi, D. Mohebbi-Kalhor and E. Ahmadi, A novel activated carbon from human hair waste: Synthesis, characterization and utilization thereof as an efficient, reusable Ni (II) adsorbent, *Curr. Res. Green Sustainable Chem.*, 2021, **4**, 100141.

76 D. N. K. P. Negara, T. G. T. Nindhia, I. W. Surata, F. Hidajat and M. Sucipta, Textural characteristics of activated carbons derived from tabah bamboo manufactured by using  $\text{H}_3\text{PO}_4$  chemical activation, *Mater. Today: Proc.*, 2020, **22**, 148–155.

77 O. Ioannidou and A. Zabaniotou, Agricultural residues as precursors for activated carbon production—A review, *Renewable Sustainable Energy Rev.*, 2007, **11**(9), 1966–2005.

78 K. Y. Foo and B. H. Hameed, Coconut husk derived activated carbon via microwave induced activation: effects of activation agents, preparation parameters and adsorption performance, *Chem. Eng. J.*, 2012, **184**, 57–65.

79 O. J. Fonseca-Bermudez, L. Giraldo, R. Sierra-Ramirez, J. Serafin, B. Dziejarski, M. G. Bonillo, *et al.*, Cashew nut shell biomass: a source for high-performance  $\text{CO}_2/\text{CH}_4$  adsorption in activated carbon, *J. CO<sub>2</sub> Util.*, 2024, **83**, 102799.

80 A. Mohan, A. Jaison, H. U. Lee, S. Park, D. Shin, J. Y. Moon, *et al.*, Facile synthesis of N-doped biomass derived porous carbon from *Opuntia humifusa* using simple solid state activation method for reversible capture of volatile iodine, *J. Anal. Appl. Pyrolysis*, 2024, **179**, 106473.

81 R. O. Gembo, S. Odisitse, T. A. M. Msagati and C. K. King'ondi, The beneficiation of asphalt waste through conversion into an efficient activated carbon adsorbent for diazinon pesticide, optimized through response surface methodology, *RSC Sustainability*, 2024, **2**(7), 2026–2042.

82 S. Yarramsetti, M. Girirajan, S. Kalluri, S. Sangaraju and P. S. Maram, Multifunctional activated carbon derived from novel biomass for high-performance energy storage applications: A sustainable alternative to fossil-fuel-derived carbon, *Mater. Chem. Phys.*, 2024, **320**, 129424.

83 D. Kumbhar, A. Palliyarayil, D. Reghu, D. Shrungar, S. Umapathy and S. Sil, Rapid discrimination of porous

bio-carbon derived from nitrogen rich biomass using Raman spectroscopy and artificial intelligence methods, *Carbon*, 2021, **178**, 792–83.

84 Jr O. F. Cruz, J. Serafin, F. Z. Azar, M. E. Casco, J. Silvestre-Albero, D. Hotza, *et al.*, Microwave-Assisted hydrothermal carbonization and characterization of Amazonian biomass as an activated carbon for methane adsorption, *Fuel*, 2024, **358**, 130329.

85 J. Serafin, B. Dziejarski, X. Vendrell, K. Kielbasa and B. Michalkiewicz, Biomass waste fern leaves as a material for a sustainable method of activated carbon production for CO<sub>2</sub> capture, *Biomass Bioenergy*, 2023, **175**, 106880.

86 V. N. Tsaneva, W. Kwapinski, X. Teng and B. A. Glowacki, Assessment of the structural evolution of carbons from microwave plasma natural gas reforming and biomass pyrolysis using Raman spectroscopy, *Carbon*, 2014, **80**, 617–628.

87 F. Ahmad, W. M. A. W. Daud, M. A. Ahmad, R. Radzi and A. A. Azmi, The effects of CO<sub>2</sub> activation, on porosity and surface functional groups of cocoa (*Theobroma cacao*)-shell based activated carbon, *J. Environ. Chem. Eng.*, 2013, **1**(3), 378–388.

88 J. Correa-Abril, U. Stahl, E. V. Cabrera, Y. J. Parra, M. A. Vega, S. Taamalli, F. Louis and J. M. Rodríguez-Díaz, Adsorption dynamics of Cd<sup>2+</sup> (aq) on microwave-synthesized pristine biochar from cocoa pod husk: Green, experimental, and DFT approaches, *iScience*, 2024, **27**(6), 109958.

89 F. Yang, C. Jin, S. Wang, Y. Wang, L. Wei, L. Zheng, *et al.*, Bamboo-based magnetic activated carbon for efficient removal of sulfadiazine: Application and adsorption mechanism, *Chemosphere*, 2023, **323**, 138245.

90 A. S. Franca, L. S. Oliveira, A. A. Nunes and C. C. O. Alves, Microwave assisted thermal treatment of defective coffee beans press cake for the production of adsorbents, *Bioresour. Technol.*, 2010, **101**(3), 1068–1074.

91 N. A. N. Mohamad and J. Jai, Response surface methodology for optimization of cellulose extraction from banana stem using NaOH-EDTA for pulp and papermaking, *Helijon*, 2022, **8**(3), e09114.

92 I. Kubovský, D. Kačíková and F. Kačík, Structural changes of oak wood main components caused by thermal modification, *Polymers (Basel)*, 2020, **12**(2), 485.

93 L. Li, G. Cao and R. Zhu, Adsorption of Cr (VI) from aqueous solution by a litchi shell-based adsorbent, *Environ. Res.*, 2021, **196**, 110356.

94 Y. Dago-Serry, K. N. Maroulas, A. K. Tolkou, N. AbdelAll, A. N. Alodhayb, G. A. Khouqueer, *et al.*, Composite super-adsorbents of chitosan/activated carbon for the removal of nonsteroidal anti-inflammatory drug from wastewaters, *J. Mol. Struct.*, 2024, **1298**, 137044.

95 Y. A. R. Lebron, V. R. Moreira, L. V. S. Santos and R. S. Jacob, Remediation of methylene blue from aqueous solution by Chlorella pyrenoidosa and Spirulina maxima biosorption: equilibrium, kinetics, thermodynamics and optimization studies, *J. Environ. Chem. Eng.*, 2018, **6**(5), 6680–6690.

96 T. Santhi, S. Manonmani, V. S. Vasantha and Y. T. Chang, A new alternative adsorbent for the removal of cationic dyes from aqueous solution, *Arabian J. Chem.*, 2016, **9**, S466–S474.

97 Z. N. Garba, W. Zhou, I. Lawan, W. Xiao, M. Zhang, L. Wang, *et al.*, An overview of chlorophenols as contaminants and their removal from wastewater by adsorption: A review, *J. Environ. Manage.*, 2019, **241**, 59–75.

98 S. K. Pereira, S. Kini, B. Prabhu and G. P. Jeppu, A simplified modeling procedure for adsorption at varying pH conditions using the modified Langmuir-Freundlich isotherm, *Appl. Water Sci.*, 2023, **13**(1), 29.

99 S. M. de Oliveira Brito, H. M. C. Andrade, L. F. Soares and R. P. De Azevedo, Brazil nut shells as a new biosorbent to remove methylene blue and indigo carmine from aqueous solutions, *J. Hazard. Mater.*, 2010, **174**(1–3), 84–92.

100 M. L. F. A. De Castro, M. L. B. Abad, D. A. G. Sumalinog, R. R. M. Abarca, P. Paoprasert and M. D. G. de Luna, Adsorption of methylene blue dye and Cu(II) ions on EDTA-modified bentonite: isotherm, kinetic and thermodynamic studies, *Sustainable Environ. Res.*, 2018, **28**(5), 197–205, DOI: [10.1016/j.serj.2018.03.001](https://doi.org/10.1016/j.serj.2018.03.001).

101 D. Pandey, A. Daverey, K. Dutta, V. K. Yata and K. Arunachalam, Valorization of waste pine needle biomass into biosorbents for the removal of methylene blue dye from water: kinetics, equilibrium and thermodynamics study, *Environ. Technol. Innovation*, 2022, **25**, 102200, DOI: [10.1016/j.eti.2021.102200](https://doi.org/10.1016/j.eti.2021.102200).

102 T. K. Sen, Adsorptive removal of dye (methylene blue) organic pollutant from water by pine tree leaf biomass adsorbent, *Processes*, 2023, **11**(7), 1877, DOI: [10.3390/pr11071877](https://doi.org/10.3390/pr11071877).

